



# A multiscale high-cycle fatigue-damage model for the stiffness degradation of fiber-reinforced materials based on a mixed variational framework

Nicola Magino<sup>a</sup>, Jonathan Köbler<sup>a</sup>, Heiko Andrä<sup>a</sup>, Fabian Welschinger<sup>b</sup>, Ralf Müller<sup>c</sup>,  
Matti Schneider<sup>d,\*</sup>

<sup>a</sup> Fraunhofer ITWM, Department of Flow and Material Simulation, Germany

<sup>b</sup> Robert Bosch GmbH, Corporate Sector Research and Advance Engineering, Germany

<sup>c</sup> University of Kaiserslautern, Institute of Applied Mechanics, Germany

<sup>d</sup> Karlsruhe Institute of Technology (KIT), Institute of Engineering Mechanics, Germany

Received 24 February 2021; received in revised form 27 August 2021; accepted 14 September 2021

Available online xxxx

## Abstract

Under fatigue-loading, short-fiber reinforced thermoplastic materials typically show a progressive degradation of the stiffness tensor. The stiffness degradation prior to failure is of primary interest from an engineering perspective, as it determines *when* fatigue cracks nucleate. Efficient modeling of this fatigue stage allows the engineer to monitor the fatigue-process prior to failure and design criteria which ensure a safe application of the component under investigation.

We propose a multiscale model for the stiffness degradation in thermoplastic materials based on resolving the fiber microstructure. For a start, we propose a specific fatigue-damage model for the matrix, and the degradation of the thermoplastic composite arises from a rigorous homogenization procedure. The fatigue-damage model for the matrix is rather special, as its convex nature precludes localization, permits a well-defined upscaling, and is thus well-adapted to model the phase of stable stiffness degradation under fatigue loading. We demonstrate the capabilities of the full-field model by comparing the predictions on fully resolved fiber microstructures to experimental data.

Furthermore, we introduce an associated model-order reduction strategy to enable component-scale simulations of the local stiffness degradation under fatigue loading. With model-order reduction in mind and upon implicit discretization in time, we transform the minimization of the incremental potential into an equivalent mixed formulation, which combines two rather attractive features. More precisely, upon order reduction, this mixed formulation permits precomputing all necessary quantities in advance, yet, retains its well-posedness in the process. We study the characteristics of the model-order reduction technique, and demonstrate its capabilities on component scale. Compared to similar approaches, the proposed model leads to improvements in runtime by more than an order of magnitude.

© 2021 The Authors. Published by Elsevier B.V. This is an open access article under the CC BY-NC-ND license (<http://creativecommons.org/licenses/by-nc-nd/4.0/>).

**Keywords:** High-cycle fatigue damage; Stiffness degradation; Short-fiber reinforced materials; Generalized standard material; Model-order reduction; Computational homogenization

\* Corresponding author.

E-mail address: [matti.schneider@kit.edu](mailto:matti.schneider@kit.edu) (M. Schneider).

## 1. Introduction

### 1.1. State of the art

To understand the complex failure behavior of structures made of fiber-reinforced composites, which might be studied experimentally [1–3] or by simulative [4,5] means, it is imperative to account for the underlying microstructure. Indeed, the introduced fillers disturb the homogeneity of the material, giving rise to natural “notch” effects at the matrix–filler interfaces from which damage may evolve.

We are interested in fiber-reinforced thermoplastic (SFRP) components under fatigue loading. Thermoplastic materials show a complex non-linear material behavior that depends on temperature, the processing conditions (e.g., on crystallinity) and the loading rate [6,7]. For high-cycle fatigue of thermoplastic composites, in contrast to most polycrystalline materials, a significant decrease of the material stiffness is observed prior to the emergence of macroscopic fatigue cracks [8]. This phenomenon is believed to be primarily driven by molecular rearrangements in the matrix (e.g., crazing) and coalescing microcracks [9,10]. This decrease of stiffness is also observed in polymer composites, and the level of stiffness loss is typically on the order of ten percent [11].

At high loading frequencies, the self-heating of the material leads to a thermally induced shift in the mechanical properties of the material [12]. Therefore, one usually restricts the load frequency to several Hz for the load amplitudes typical for high-cycle fatigue [13,14]. The resulting temperature increase does not exceed 3–5 K [15], so that thermally induced fatigue can be neglected. For mechanics-driven fatigue, the dependence of the material behavior on the frequency is less pronounced.

The most common damage mechanisms in short-fiber reinforced polymers are fiber fracture, fiber pull-out, matrix damage and failure at the matrix–fiber interface [16]. Microvoids in the matrix are consistently reported to contribute to the material damage significantly [17–20]. Under fatigue loading, the number of microvoids increases not only in regions of high stress, such as at the fiber tips [17,20], but also in zones of low fiber density [20]. Starting from these microvoids, microcracks start to form at the fiber tips and alongside the fibers. Belmonte et al. [17] report these primary microvoids to form several tenths of a micrometer away from the matrix–fiber interface. This observation indicates that matrix failure represents the dominant damage mechanism. Other authors report adhesive fracture at the interface (matrix–fiber failure) [18,19] or both failure modes [20]. These differences may be due to different chemical coatings used by the supplier to improve the fiber–matrix adhesion [17]. From a macroscopic perspective, several authors [21–24] identified three stages of evolving fatigue damage in thermoplastic composites. An initially rapid decrease of the stiffness is followed by a stable phase of fatigue-damage evolution, and a phase of final failure.

Modeling strategies for the fatigue of polymer composites encompass phenomenological progressive damage models and physics-based progressive damage models. The former model damage growth based on macroscopic observable properties and thus require extensive (typically rather costly) experimental studies [22–26]. The second approach accounts for fatigue effects on the microstructure, such as matrix damage, fiber fracture and matrix–fiber debonding, explicitly. The macroscopic material behavior emerges by homogenization in a natural way, see Matouš et al. [27] for a recent overview on computational homogenization methods. Mean-field techniques [28] for fatigue modeling of fiber reinforced polymers were developed by Krairi et al. [29] and Kammoun et al. [30]. Moreover, Jain et al. [31,32] consider a master S/N-curve approach based on a mean-field model. More precisely, they account for damage on the microscopic scale via fiber–matrix debonding and assess final failure via a criterion based on the amount of stiffness degradation, which is assumed to be independent of the fiber orientation. Jain et al. [31] reported their method to be fast, reliable and more accurate than established methods, e.g., based on empirical reduction coefficients [33–35] and rescaling based on the tensile strength [36–40]. These analytical methods are complemented by computational approaches. Developed for general two-scale problems, the FE<sup>2</sup> method [41] associates a finite-element model of the microstructure to every integration point of the macroscale. In the context of damage in composite structures, the method was successfully applied [42,43]. To speed up the computations on the microscale, methods based on the fast Fourier transform (FFT) [44,45] were used to replace the finite element models on the microscale, giving rise to the FE-FFT method [46–48], and applied to damage in short-fiber reinforced composites [46]. To further reduce the computational burden of the simulations, model-order reduction (MOR) strategies prove useful, like the transformation-field analysis of Dvorak and coworkers [49,50], its nonuniform extension [51–53] and the self-consistent clustering analysis [54–56]. Alternatively, machine-learning methods [57–63] may be used for multiscale simulations.

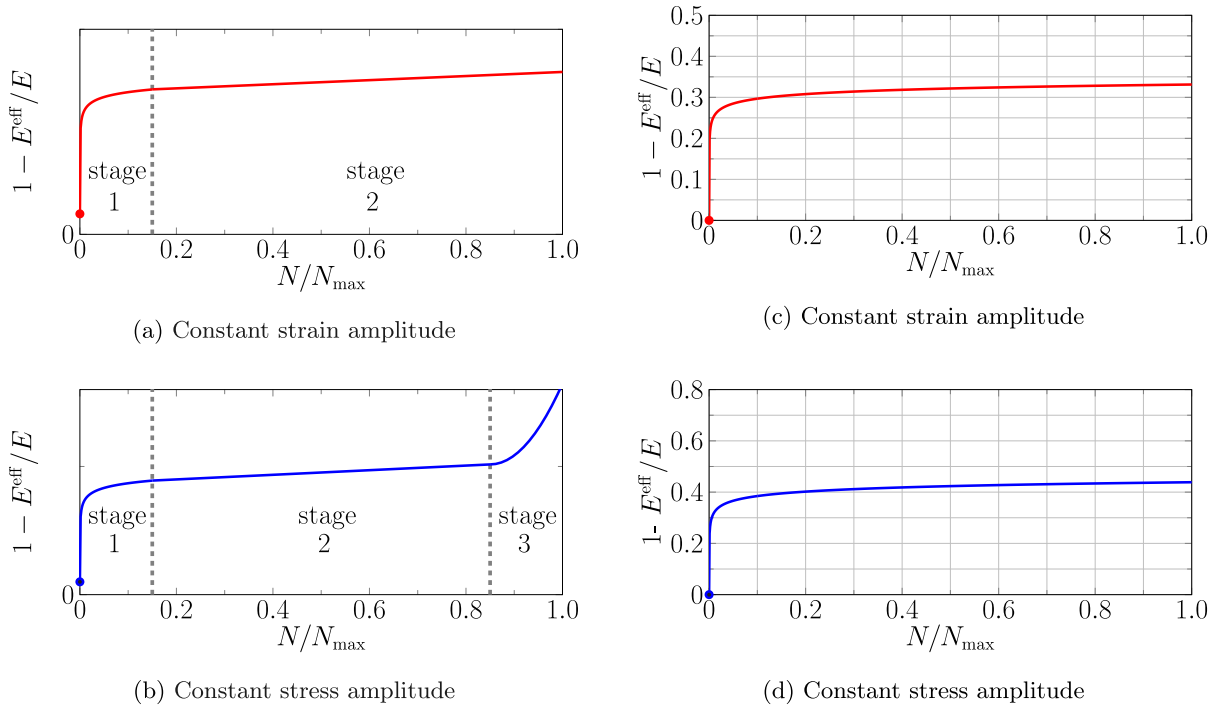


**Fig. 1.** Comparison of the effective fatigue damage reported in the literature [23] (left) and predicted by the proposed model (right), distinguishing constant strain amplitude (top) and constant stress amplitude (bottom) for reversible loading (i.e.,  $R = 0$ ).

Recently, Köbler et al. [64] proposed an efficient multiscale fatigue-damage model for short-fiber reinforced thermoplastics based on a modification of classical phase-field fracture [65–67], combined with non-uniform transformation-field analysis (NTFA) [51–53] and fiber-orientation interpolation [68]. After an implicit discretization in time, the incremental potential of the model is a fourth-order polynomial in the involved fields. In particular, a precomputation strategy could be used to speed up the online evaluation, enabling component-scale simulations. The MOR ansatz of Köbler et al. [64] and the mean-field approach of Jain et al. [31] share a common strategy. First, the stable phase of fatigue damage is modeled. Then, a failure criterion based on the relative stiffness degradation is utilized for predicting the fracture cycle. However, both articles differ in the computational approach to the microscale, with mean-field [31] and full field/MOR [68] models representing the different strategies.

### 1.2. Contributions

This work builds upon the approach introduced by Jain et al. [31] and refined in Köbler et al. [64] in terms of a suitable multiscale fatigue-damage model of short-fiber polymer composites. Following their strategy, we are interested in modeling the progressive stiffness degradation in the stable phase prior to failure, serving as the basis of a subsequent failure assessment via an appropriate criterion. To be more precise, we introduce a scalar fatigue-damage model for the polymer matrix, and the stiffness degradation of the composite arises from a suitable MOR strategy in a computational homogenization framework.

Köbler et al. [64] used a fatigue-damage model that is quite similar to classical phase-field fracture models [65–67] and exploited the fact that the corresponding incremental potential is a fourth-order polynomial in the involved fields, which permits to express the incremental potential in a MOR framework *exactly* in terms of suitable precomputed quantities. In particular, no special quadrature [69] is necessary in the NTFA procedure.

Taking a closer look at the typical stiffness degradation of polymer composites upon fatigue loading [21,23], see Fig. 1, we notice that the first and the second phase of the fatigue-damage evolution on the macroscale are characterized by a steady and stable damage evolution. Only for prescribed stress amplitude and in the third, final phase, localization occurs. As the models of Jain et al. [31] and Köbler et al. [64] only require modeling the

first and the second phase of the fatigue-damage evolution to assess the lifetime of the component, we sought an alternative damage model which permits a more efficient numerical treatment. Indeed, to model this stable phase, it appears sufficient to employ a fatigue-damage model which avoids the negative side effects of softening damage models, like the inherently high number of modes necessary to capture the evolution in the strain softening regime appropriately [64, Fig. 21] and the loss of representativity upon softening [70].

For this purpose, we build upon the convex, rate-independent damage model [71,72] of Görthofer et al. [73]. Inspired by the work of Govindjee [74], Görthofer et al. [73] proposed a framework for damage models that directly operates on the compliance matrix as an internal variable and satisfies Wulfinghoff's damage criterion [75]. The resulting strain energy is jointly convex in the strain and internal variables and thus precludes strain softening [76], leading to mesh-independent results without the necessity of introducing a gradient term of the damage variable [77–83]. In contrast to elastoplastic models, which may be used for modeling a shift in the "secant stiffness", our approach permits to predict the degradation of the full stiffness tensor, accounting for anisotropy effects.

To reproduce the characteristic behavior of the fatigue-damage evolution in the first two stages, see Fig. 1, we formulate the model in the *logarithmic cycle* space. In addition to closely matching what is observed in experiments, see Fig. 1, this formulation leads to a high computational efficiency, as a large number of cycles can be simulated quickly. Endowing the thermoplastic matrix with this model leads to a naturally emerging multiscale model, see Section 2.2, which we demonstrate to be appropriate to capture the loss of stiffness upon fatigue loading for a glass–fiber reinforced polybutylene terephthalate (PBT), see Section 2.3, at least if the stiffness reduction introduced in the initial phase, which can be determined experimentally with little effort, is considered.

Unfortunately, in its original form, the introduced fatigue-damage model is not directly suitable for efficient model-order reduction. In contrast to the model of Köbler et al. [64], the class of models introduced by Görthofer et al. [73] leads to an incremental potential whose integrand is no longer a polynomial in the fields. In particular, the precomputing strategy of Köbler et al. [64] does not apply. Of course, approximation procedures [84,85], Gauss quadrature [69] or polynomialization [86] could be applied. To avoid the resulting decrease in accuracy or increase in computational effort, we follow a different route. More precisely, we exploit a reformulation of the fatigue-damage evolution in terms of the stress amplitude. Mathematically speaking, we apply a partial Legendre transform in the strain amplitude. By this nonlinear transformation, the underlying saddle-point problem has an incremental potential which is a third-order polynomial in the involved stress-amplitude and fatigue-damage field. In particular, the precomputation strategy of Köbler et al. [64] applies. However, this reformulation comes at a cost. The original, primal minimization principle is replaced by a mixed variational principle, and its structure needs to be studied anew, in particular concerning model-order reduction. Fortunately, see Section 3 for details, the corresponding mixed variational principle turns out to be well-posed, even upon model-order reduction, as long as suitable (physically sound) conditions hold. We thoroughly investigate the sensitivity of the multiscale model and its reduced-order model w.r.t. the involved parameters in Section 4, and demonstrate the capabilities of the ensuing model on component scale, see Section 5.

## 2. A fatigue-damage model for the stiffness degradation

In Section 2.1, we introduce a (homogeneous) material model for the polymer matrix which models the stiffness degradation upon fatigue loading. The material model may appear simple, but was selected with its favorable properties concerning model-order reduction in mind.

Köbler et al. [64] work directly in cycle space for reasons of efficiency. In a similar direction, we consider a time-like variable directly in *logarithmic cycle* space. We investigate the material behavior in a one-dimensional stress- and strain-driven load case and compare the material behavior to fatigue degradation of short-fiber reinforced polymers reported in the literature [22,23,87]. Subsequently, in section 2.2, the described model enters as a constituent in a composite, mathematically encoded by an appropriate first-order homogenization framework. Upon discretization in cycle space and for prescribed stress (amplitude), we also discuss the naturally associated variational principle. We close this section by showing that the introduced model captures the phase of second, stable stiffness degradation of fiber-reinforced composite microstructures quite accurately, at least if the initial stiffness degradation is accounted for.

### 2.1. Matrix modeling

We introduce a fatigue-damage material model at small strains using the framework of generalized standard materials (GSMs) of dissipative solids [88,89]. We formulate our model in logarithmic cycle space, described by a continuous variable  $\bar{N} \geq 0$ , instead of the more standard *time* framework. To be precise, we use the rescaling  $\bar{N} = \log_{10}(N)$  throughout this work, where  $N$  refers to the current cycle, and introduce a time like derivative  $q' \equiv dq/d\bar{N}$ . This choice permits taking large steps  $\Delta\bar{N}$  in logarithmic cycle space, necessary for treating high-cycle fatigue problems, instead of small time steps  $\Delta t$ . The GSM framework is carried over to the cycle setting, by simply relabeling the time  $t$  by the cycle  $\bar{N}$  (some care has to be taken with the dimensions, as the time-like scale  $\bar{N}$  is dimensionless).

The proposed model involves a scalar damage variable  $d \geq 0$  as the only internal variable. We consider the free energy

$$w(\varepsilon, d) = \frac{1}{2(1+d)} \varepsilon : \mathbb{C} : \varepsilon, \tag{2.1}$$

where  $\varepsilon$  refers to the elastic (small) strain tensor and  $\mathbb{C}$  denotes the (undamaged) fourth-order stiffness tensor. The model is completed by the dissipation potential

$$\phi(d') = \frac{1}{2\alpha} (d')^2, \tag{2.2}$$

where  $\alpha > 0$  determines the speed of evolution and  $d'$  denotes the derivative of the fatigue-damage variable  $d$  w.r.t. the continuous logarithmic cycle variable  $\bar{N}$ . The associated Cauchy stress-tensor  $\sigma$  is defined by

$$\sigma \equiv \frac{\partial w}{\partial \varepsilon}(\varepsilon, d) = \frac{1}{(1+d)} \mathbb{C} : \varepsilon, \tag{2.3}$$

i.e., the stiffness tensor is reduced by a factor  $1/(1+d)$  for growing fatigue-damage variable  $d$ . Biot's equation associated to the described model reads

$$0 \stackrel{!}{=} \frac{\partial w}{\partial d}(\varepsilon, d) + \frac{\partial \phi}{\partial d'}(d') = -\frac{1}{2(1+d)^2} \varepsilon : \mathbb{C} : \varepsilon + \frac{d'}{\alpha}, \tag{2.4}$$

i.e., in explicit form

$$d' = \frac{\alpha}{2(1+d)^2} \varepsilon : \mathbb{C} : \varepsilon. \tag{2.5}$$

As the right-hand side is always non-negative, the damage variable is non-decreasing for increasing cycles  $\bar{N}$ .

An implicit Euler discretization of Eq. (2.5) in logarithmic cycle space leads to the equation

$$\frac{d^{n+1} - d^n}{\Delta\bar{N}} = \frac{\alpha}{2(1+d^{n+1})^2} \varepsilon : \mathbb{C} : \varepsilon, \tag{2.6}$$

where  $d^n$  refers to the damage value at the previous and  $d^{n+1}$  to the damage value at the current state.

To gain some understanding of the predictions made by the model, we shall discuss uniaxial extension for the one-dimensional case in more detail. In this context, we denote the Young's modulus by  $E$ .

For a constant peak stress  $\sigma_{\max}$ , the differential equation (2.5) with initial condition  $d(0) = 0$  may be integrated exactly,

$$d(\bar{N}) = \frac{\alpha}{2} \frac{\sigma_{\max}^2}{E} \bar{N}. \tag{2.7}$$

Thus, the damage variable  $d$  grows linearly in the variable  $\bar{N}$ . In Fig. 2(a), the solution is plotted for a stress amplitude of  $\sigma_{\max} = 25$  MPa and the Young's modulus  $E = 3$  GPa. The fatigue-damage variable depends linearly on the parameter  $\alpha$ , resulting in a faster evolution of the damage variable  $d$  with increasing  $\alpha$ . The damage variable has no upper bound and evolves towards  $+\infty$  under fatigue loading. This corresponds to an asymptotic degradation of the effective stiffness  $E^{\text{eff}} = \frac{1}{1+d} E$  towards zero,

$$E^{\text{eff}} = \frac{1}{1 + \frac{1}{2}\alpha\sigma_{\max}^2\bar{N}/E} E, \tag{2.8}$$

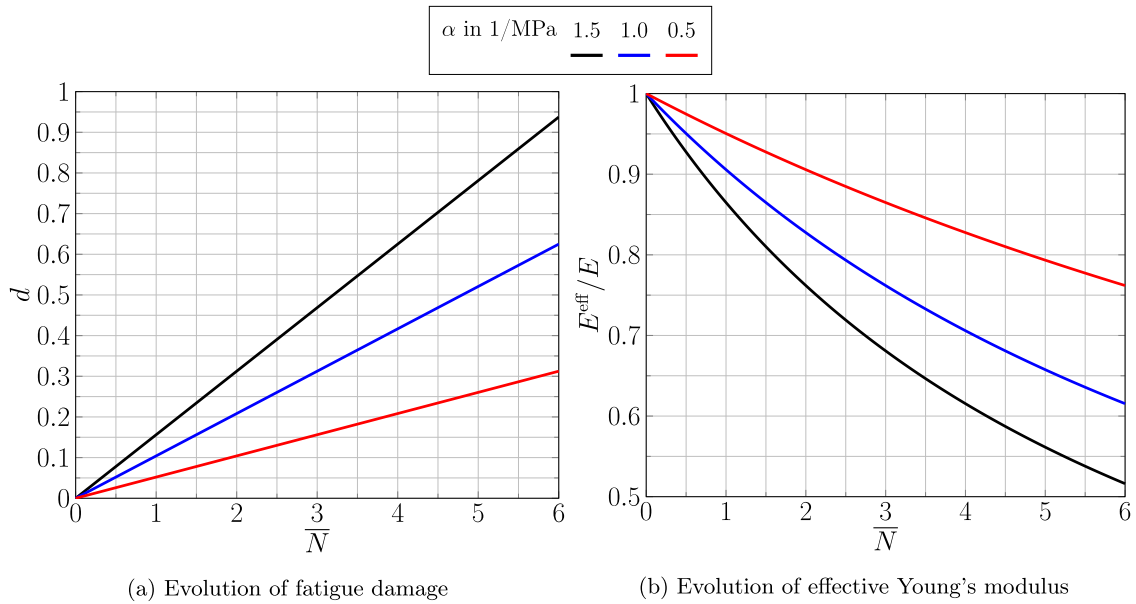


Fig. 2. Effect of changing the parameter  $\alpha$  on the model for constant stress amplitude  $\sigma_{\max} = 25$  MPa.

as shown in Fig. 2(b). At the undamaged state  $d = 0$ , the current effective Young's modulus  $E^{\text{eff}}$  equals the elastic modulus  $E$ . Under fatigue loading, the effective Young's modulus decreases. The slope of the  $E-\bar{N}$ -curve decreases with increasing  $\bar{N}$ . Thus, for high number of cycles, the degradation of the effective Young's modulus is slowed down. Indeed, since the damage variable  $d$  never reaches  $+\infty$ , the state  $E = 0$  of the material is not reached.

For a constant peak strain  $\varepsilon_{\max}$  and the initial condition  $d(0) = 0$ , the damage evolution integrates to the expression

$$d(\bar{N}) = \left(1 + \frac{3\alpha}{2} E \varepsilon_{\max}^2 \bar{N}\right)^{\frac{1}{3}} - 1. \tag{2.9}$$

The solution is plotted for a strain amplitude of  $\varepsilon_{\max} = 8.33 \times 10^{-3}$  and a Young's modulus of  $E = 3$  GPa in Fig. 3(a). The corresponding evolution of the effective Young's modulus

$$E^{\text{eff}} = \frac{1}{\left(1 + \frac{3}{2}\alpha E \varepsilon_{\max}^2 \bar{N}\right)^{\frac{1}{3}}} E \tag{2.10}$$

is shown in Fig. 3(b). The exponent in the evolution of the damage variable of  $1/3$  is smaller than under constant stress, where the exponent is one. Still, as for stress loading, the fatigue damage evolution grows to  $+\infty$  as  $\bar{N} \rightarrow +\infty$ . Under constant strain amplitude, the evolution of the effective Young's modulus asymptotically goes to zero, as well. However, due to the cubic root-type evolution of the damage variable under constant strain amplitude compared to the linear evolution under constant stress amplitude, the degradation of the material progresses at a slower rate.

Both under constant stress and constant strain amplitude, the model does not feature a fatigue limit. Instead, the model predicts a stable stiffness degradation to zero, due to fatigue damage. To predict the complete failure upon fatigue loading, an additional failure criterion needs to be supplemented.

In Fig. 1, the introduced fatigue-damage model is compared to typical experimental results from the literature. The stiffness evolution of the proposed model is given for  $\alpha = 1.5$   $1/\text{MPa}$  and a Young's modulus of  $E = 3$  GPa. The loadings are chosen with a stress amplitude of  $\sigma_a = 25$  MPa and a strain amplitude of  $\varepsilon_{\max} = 8.33 \times 10^{-3}$ . In strain-controlled fatigue experiments of short-fiber reinforced polymers, two distinct stages emerge in cycle space. Starting from an initial damage value evoked by the preloading step (and whose magnitude depends on the applied

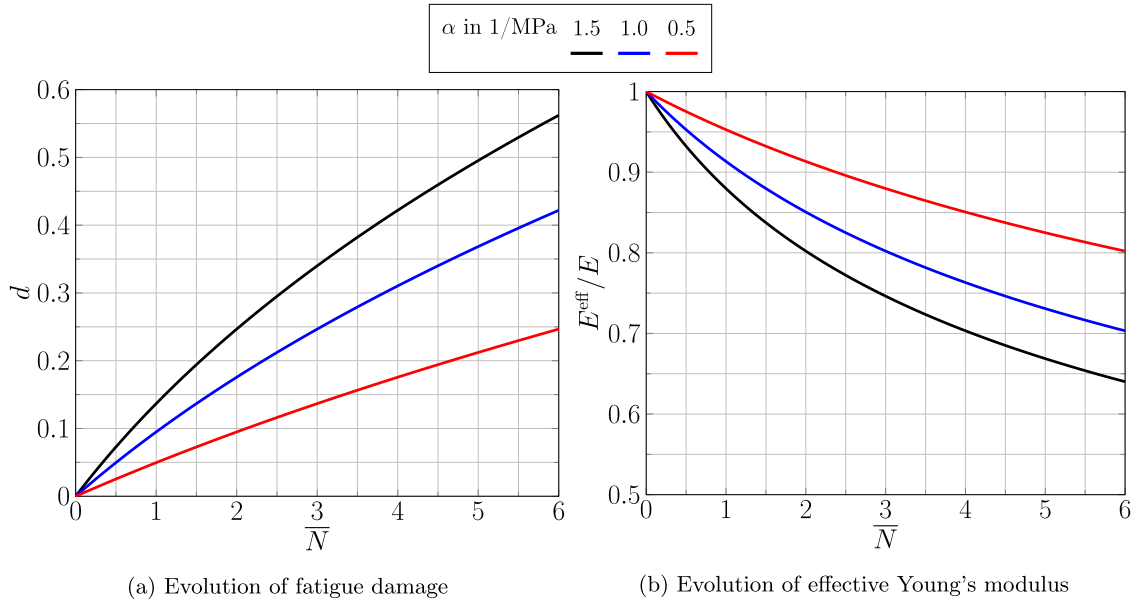


Fig. 3. Effect of the parameter  $\alpha$  on the model for constant strain amplitude  $\varepsilon_{\max} = 8.33 \times 10^{-3}$ .

displacement [23]), the stiffness decreases rapidly in the first stage of fatigue loading. The proposed fatigue-damage model may reproduce the initial loss in stiffness by considering a positive initial value  $d_0 > 0$ . If  $d_0 = 0$  is used, the stiffness degradation experienced in the first cycle will not be accounted for. The model at hand qualitatively reproduces the rapid degradation of the material in stage-1 fatigue. Subsequently, in experimental stage-2 fatigue, the material degradation enters a stable phase of stiffness degradation. The effective Young's modulus of the material decreases gradually. The model at hand may reproduce this fatigue-loading regime quite accurately.

Under constant stress-amplitude loading, the stiffness degradation is also characterized by these two phases, but enters a third stage, which was not observed for displacement-driven experiments. In this third stage, a critical damage state forms which leads to a complete fracture of the test specimen. This stage-3 fatigue is not accounted for by the proposed fatigue model on the microscale. Rather, the onset of macroscopic failure can be determined via a suitable failure criterion, like a prescribed amount of stiffness lost [31,32,64].

### 2.2. Model on the microscale

Consider a cubic cell  $Y \subseteq \mathbb{R}^m$ , and suppose that a microscopic stiffness distribution  $Y \ni x \mapsto \mathbb{C}(x)$ , associating a (non-degenerate) linear elastic stiffness tensor to each microscopic point, and a (bounded) field  $\alpha : Y \rightarrow [0, \infty)$ , are given. For a prescribed path of macroscopic stress amplitudes

$$\Sigma : [0, \bar{N}_{\max}] \rightarrow \text{Sym}(m), \tag{2.11}$$

mapping into the space  $\text{Sym}(m)$  of symmetric  $m \times m$  tensors, we seek a displacement fluctuation field  $u$ , a strain field  $\varepsilon$ , a stress field  $\sigma$  and a damage field  $d$ , all defined on the microscopic scale, satisfying kinematic compatibility

$$\varepsilon(\bar{N}, x) = \langle \varepsilon(\bar{N}, \cdot) \rangle_Y + \nabla^s u(\bar{N}, x), \tag{2.12}$$

where  $\langle \cdot \rangle_Y$  stands for averaging over the cell  $Y$ , the constitutive equation

$$\sigma(\bar{N}, x) = \frac{1}{(1 + d(\bar{N}, x))} \mathbb{C}(x) : \varepsilon(\bar{N}, x), \tag{2.13}$$

the (quasi-static) balance of linear momentum

$$\text{div } \sigma(\bar{N}, x) = 0 \tag{2.14}$$

and Biot's equation

$$d'(\bar{N}, x) = \frac{\alpha(x)}{2(1+d(\bar{N}, x))^2} \varepsilon(\bar{N}, x) : \mathbb{C}(x) : \varepsilon(\bar{N}, x), \quad (2.15)$$

together with the prescribed stress amplitude  $\Sigma(\bar{N})$

$$\langle \sigma(\bar{N}, \cdot) \rangle_Y = \Sigma(\bar{N}) \quad (2.16)$$

and the initial condition

$$d(0, x) = 0 \quad (2.17)$$

for all  $x \in Y$ . Upon an implicit discretization in time and eliminating all fields except for  $\bar{\varepsilon}^n$ ,  $u^n$  and  $d^n$ , where the macroscopic strain  $\bar{\varepsilon}^n$  at cycle  $\bar{N}^n$  is defined as

$$\bar{\varepsilon}^n = \left\langle \varepsilon(\bar{N}^n, \cdot) \right\rangle_Y, \quad (2.18)$$

the latter set of equations, at the current cycle step, corresponds to a critical point of the variational principle

$$F^{n+1}(\bar{\varepsilon}, u, d) \longrightarrow \min \quad (2.19)$$

for the Ortiz–Stainier functional [90,91]

$$F^{n+1}(\bar{\varepsilon}, u, d) = \left\langle \frac{1}{2(1+d)} (\bar{\varepsilon} + \nabla^s u) : \mathbb{C} : (\bar{\varepsilon} + \nabla^s u) + \frac{1}{2\alpha\Delta\bar{N}} (d - d^n)^2 \right\rangle_Y - \bar{\varepsilon} : \Sigma^{n+1}. \quad (2.20)$$

For the latter definition, we use the convention that  $F^{n+1}(\bar{\varepsilon}, u, d) = +\infty$  if  $\alpha(x) = 0$  and  $d(x) \neq d^n(x)$  for  $x \in Y$ . Also, the short-hand notation  $\Sigma^n = \Sigma(\bar{N}^n)$  is used.

For the article at hand, we are primarily interested in the evolution of the *effective* stiffness upon fatigue loading. The latter arises from the local stiffness tensor field  $\mathbb{C}/(1+d)$  by linear elastic homogenization [92].

If  $\mathbb{C}$  is uniformly positive and bounded and  $\alpha$  is bounded as well, it is not difficult to see that the problem (2.20) admits a unique minimizer in a suitable Sobolev space [93]. Indeed, eliminating the damage variable  $d$  via Biot's equation (2.6) leads to a strictly convex optimization problem in the strain field, whose condensed energy grows with an exponent between 4/3 and 2 in the strain, depending on whether  $\alpha$  vanishes or not. Once the strain field is obtained, the (square-integrable) damage field may be recovered via Biot's equation.

Thus, the presented model is well-defined for Sobolev spaces with exponents larger than one. In particular, by construction, no damage localization is permitted by the mathematical model. Indeed, such localization behavior is typically observed for energies with linear growth in the strain. The superlinear growth of the condensed energy precludes localization. Thus, focusing on the stable fatigue damage regime, see stage-1 and stage-2 fatigue in Fig. 1, the presented damage model comes with a beneficial numerical treatment, as it leads to mesh-independent results also without gradient enrichment. Physically speaking, the model at hand monitors the phase of stiffness decrease which does not (yet) have fracture mechanical ramifications. This contrasts with comparable models [64].

### 2.3. Parameter identification

After discussing the ability of the model to reproduce the typical fatigue-damage behavior of short-fiber reinforced polymers in the one-dimensional case, see Section 2.1, this section is devoted to identifying the single free parameter  $\alpha$ , which governs the speed of fatigue-damage growth for the model at hand. We compare experimental results to simulations on representative volume elements (RVE) to determine this parameter. Moreover, the capability of the model to reproduce the stiffness decrease is further discussed.

We performed experiments on specimens made of polybutylene terephthalate (PBT) reinforced by E-glass fibers. The isotropic elastic moduli for these materials are given in Table 1. The elastic properties of the E-glass fibers are standard, whereas the elastic properties of the polymer matrix were identified via quasi-static testing of the pure matrix material using so-called Becker samples, see [94], on a Zwick universal testing machine. We restrict ourselves to stress ratios

$$R = \frac{\Sigma_{\min}}{\Sigma_{\max}} \quad (2.21)$$

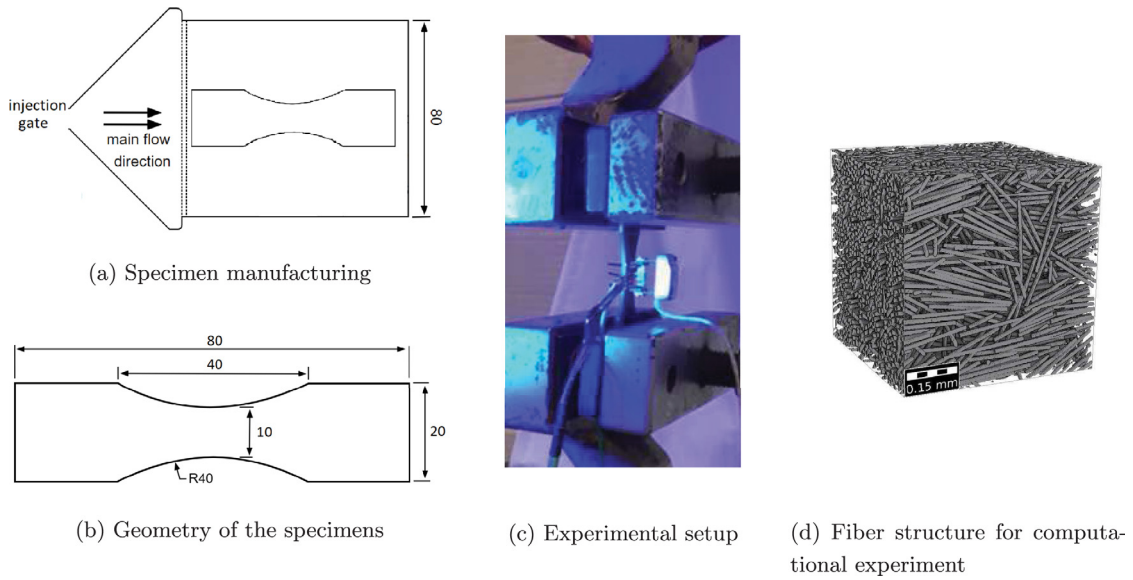


Fig. 4. Setup and geometries for experiments.

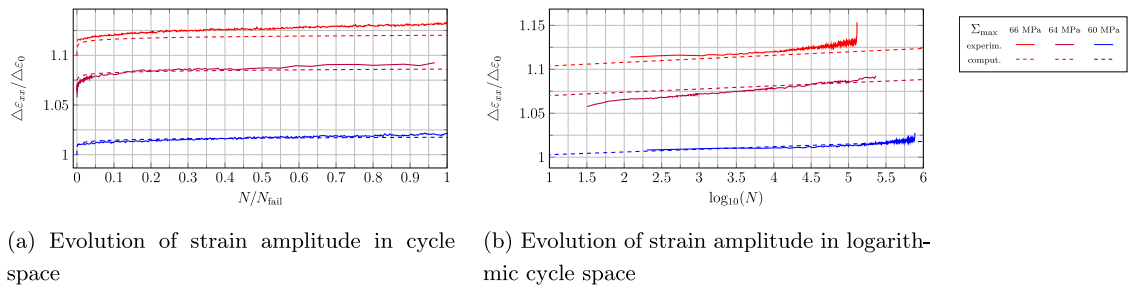


Fig. 5. Comparison of experimental data and simulation results.

**Table 1**  
Model parameters adjusted to experimental data.

Material	$E$ in GPa	$\nu$	Additional parameters
E-glass fibers	72	0.22	–
PBT matrix	2.69	0.4	$\alpha = 15$ 1/GPa

of  $R = 0$  throughout this work.

The specimens used for the fatigue tests were cut from an injection-molded plate as shown in Fig. 4(a). Each specimen has a thickness of 2 mm and the geometric properties of the specimens are shown in Fig. 4(b).

The fatigue tests were performed on a Schenk hydropulser as shown in Fig. 4(c). With respect to time-efficient testing, the frequencies of the experiments were chosen in the range from 2 Hz to 12 Hz depending on the loading amplitudes. Of course, induced self-heating of the samples limits the maximum frequency that can be applied. The chosen frequency ensures that the temperature increase during testing, measured at the sample surface, does not exceed 2 K. For the positioning of the temperature sensor on the sample, see Fig. 4(c). The local deformation in the middle of the sample is recorded using extensometers with a gauge length  $l_0 = 10$  mm, see Fig. 4(c).

In accordance with the literature [18,23,87], the experiments show an initial rapid decrease of the stiffness for low cycles and a secondary steady regime in the linear cycle space, see Fig. 5(a). The strain results are normalized by a reference strain  $\varepsilon_0$ , more precisely  $\varepsilon_0 = \varepsilon_{xx}(\bar{N} = 0)$  at a stress amplitude of 60 MPa. This decrease corresponds to a linear evolution when displayed in logarithmic cycle space, see Fig. 5(b).

For parameter identification using numerical computations on representative volume elements, it is necessary to characterize the fiber orientation state of the experimental specimens. Thus, the microstructural properties of the specimens were examined via high-resolution X-ray microcomputed tomography ( $\mu$ CT) analysis. For details of the characterization process, we refer to Hessman et al. [3]. The fiber volume content was found to be 17.8%. The identified aspect ratio depends on the segmentation algorithm and the chosen batch. The algorithm proposed by Hessman et al. [3] predicts an aspect ratio of 26.1, whereas the aspect ratio obtained from the commercial Simpleware ScanIP software is 23.9. As such small changes in the fibers' aspect ratio have little influence on the effective material behavior, we use the aspect ratio of 25 for the numerical simulations throughout this work.

The fiber orientations in these specimens show a layered structure over the thickness. To keep the procedure simple, we consider a homogeneous, averaged fiber orientation and compute the second-order Advani–Tucker tensor from the scan over the complete specimen thickness. The second-order Advani–Tucker fiber-orientation tensor  $A$  [95] is computed from the fiber directions  $p_i \in \mathcal{S} := \{p \in \mathbb{R}^3, \|p\| = 1\}$  via the formula

$$A = \frac{1}{N_{\text{fiber}}} \sum_{i=1}^{N_{\text{fiber}}} p_i \otimes p_i. \tag{2.22}$$

The obtained eigenvalues in the specimens are  $\lambda_1 = 0.770$ ,  $\lambda_2 = 0.213$  and  $\lambda_3 = 0.017$ . We use these parameters to generate the microstructure in Fig. 4(d) by the sequential addition and migration algorithm [96].

Subsequently, the microstructure shown is subjected to uni-axial extension in the principal fiber direction at the same stress amplitudes that were used in the experiment. We identified the parameter  $\alpha = 0.015$  1/MPa. In Fig. 5, we compare the measurements to numerical experiments for using a log-cycle scale  $\bar{N}$ .

For the stress amplitudes at hand, the strain evolution curves are captured quite well by the model. Both the slopes of the strain evolution as well as the initial strain amplitude, corresponding to the strain amplitude at the first cycle, are captured. However, for computations at higher or lower stress amplitudes than shown here, the initial strain amplitudes at the first cycle deviate from the experimental results. This kind of initial stiffness decrease in the first few cycles prior to stage-1 fatigue shown in Fig. 1(b) is not accounted for by the proposed model.

For the work at hand, we focus on the region between initial damage (or plastic deformation) and fracture, namely stage-1 and stage-2 fatigue. The prediction of the initial strain amplitude decrease is left for subsequent work.

The damage evolution in the fatigue damage region between initial loading and final fracture has been observed to be of logarithmic character. The formulation of the model at hand in log-cycle space  $\bar{N}$  is thus reasonable.

### 3. A model-order reduction strategy based on a mixed formulation

#### 3.1. A reformulation in terms of the stress

In the previous section we formulated our model based on the Ortiz–Stainier potential (2.20)

$$F(\bar{\varepsilon}, u, d) = \left\langle \frac{1}{2(1+d)} (\bar{\varepsilon} + \nabla^s u) : \mathbb{C} : (\bar{\varepsilon} + \nabla^s u) + \frac{1}{2\alpha \Delta \bar{N}} (d - d^n)^2 \right\rangle_Y - \bar{\varepsilon} : \Sigma, \tag{3.1}$$

where we drop the superscript  $n+1$  for this section. This formulation is not ideally suited for model-order reduction. For a basis of preselected modes, we would like to express the functional to be minimized in terms of quantities that can be precomputed, avoiding any access to full fields. However, such a precomputation is not possible, as the damage variable  $d$  enters the denominator in the Ortiz–Stainier potential. Instead of relying upon an approximation, for instance by a Taylor polynomial [69,84,85], we follow a different route.

Let us invert the stress–strain relationship (2.3) of the matrix model,

$$\varepsilon = (1+d) \mathbb{S} : \sigma \tag{3.2}$$

in terms of the compliance tensor  $\mathbb{S} = (\mathbb{C})^{-1}$ . Similarly, we may recast Biot's equation (2.5) in the form

$$d' = \frac{\alpha}{2} \sigma : \mathbb{S} : \sigma, \quad \text{or,} \quad \frac{d - d^n}{\Delta \bar{N}} = \frac{\alpha}{2} \sigma : \mathbb{S} : \sigma \tag{3.3}$$

upon an implicit Euler discretization in logarithmic cycle space. With precomputations useful for model-order reduction in mind, this reformulation is very convenient. Indeed, Eqs. (3.2) and (3.3) involve only terms that are

jointly quadratic in the internal variables  $(\sigma, d)$ . A lower degree of homogeneity in the joint internal variables is favorable for precomputations, as this degree affects the number of the precomputed system matrices in the reduced order model, see Section 3.2.

As for the primal model, see section equations (2.1) and (2.2), we may establish a (mixed) variational principle

$$S(\sigma, d) \longrightarrow \min_d \max_{\substack{\text{div } \sigma = 0 \\ \langle \sigma \rangle_Y = \Sigma}} \quad (3.4)$$

in terms of the saddle-point function

$$S(\sigma, d) = \left\langle -\frac{(1+d)}{2} \sigma : \mathbb{S} : \sigma + \frac{1}{2\alpha\Delta N} (d - d^n)^2 \right\rangle_Y. \quad (3.5)$$

The equivalence of the strain- and the stress-based formulations, (2.19) and (3.4), respectively, in terms of the relation (3.2) is shown in Appendix A. However, some care has to be taken with this formulation. Please notice that the function  $S$  is always convex in  $d$ , but concavity in  $\sigma$  is only ensured for  $d \geq -1$ . Thus, instead of the formal mixed variational principle (3.4), it is recommended to fix some  $d_- \in (-1, 0]$  and to consider the constrained mixed variational principle

$$S(\sigma, d) \longrightarrow \min_{d \geq d_-} \max_{\substack{\text{div } \sigma = 0 \\ \langle \sigma \rangle_Y = \Sigma}} \quad (3.6)$$

instead. Please notice that the considered mixed variational principle differs from the mixed variational principle of Fritzen–Leuschner [53]. Indeed, we perform a partial Legendre transform in the strain, whereas Fritzen–Leuschner rely upon a partial Legendre transform in the internal variable.

Suppose that  $M_d$  damage modes

$$\delta_a : Y \rightarrow \mathbb{R}, \quad a = 1, \dots, M_d, \quad (3.7)$$

and  $M_\sigma$  stress modes

$$s_i : Y \rightarrow \text{Sym}(m), \quad i = 1, \dots, M_\sigma, \quad (3.8)$$

satisfying

$$\langle s_i \rangle_Y = 0 \quad \text{and} \quad \text{div } s_i = 0, \quad i = 1, \dots, M_\sigma, \quad (3.9)$$

are given. Then, for  $M = (M_\sigma, M_d)$ , and coefficients

$$\vec{d} = (d_1, \dots, d_{M_d}) \in \mathbb{R}^{M_d} \quad \text{and} \quad \vec{\sigma} = (\sigma_1, \dots, \sigma_{M_\sigma}) \in \mathbb{R}^{M_\sigma}, \quad (3.10)$$

we consider the reduced-order model determined by the mixed variational principle (3.6)

$$S_M(\vec{\sigma}, \vec{d}) \longrightarrow \min_{\vec{d}, d \geq d_-} \max_{\vec{\sigma}} \quad (3.11)$$

involving the function

$$S_M(\vec{\sigma}, \vec{d}) \equiv S(\sigma, d) \quad \text{with} \quad \sigma = \Sigma + \sum_{i=1}^{M_\sigma} \sigma_i s_i \quad \text{and} \quad d = \sum_{a=1}^{M_d} d_a \delta_a, \quad (3.12)$$

and where the previous cycle step is represented in the form

$$d^n = \sum_{a=1}^{M_d} d_a^n \delta_a \quad \text{for a suitable} \quad \vec{d}^n \in \mathbb{R}^{M_d}. \quad (3.13)$$

Notice that, in the reduced-order setting, it is not readily apparent that the problem (3.11) is solvable, and that there is a unique solution. For this purpose, let us introduce the non-linear operator

$$\mathcal{A}_M : \mathbb{R}^{M_\sigma} \times \mathbb{R}^{M_d} \rightarrow \mathbb{R}^{M_\sigma} \times \mathbb{R}^{M_d}, \quad (3.14)$$

implicitly defined via

$$\left\langle \mathcal{A}_M \left( \vec{\sigma}^\beta, \vec{d}^\beta \right), \left( \vec{\sigma}^\gamma, \vec{d}^\gamma \right) \right\rangle_M = \left\langle \left( 1 + d^\beta \right) \left( \Sigma + \sigma^\beta \right) : \mathbb{S} : \sigma^\gamma + \frac{1}{\alpha \Delta N} \left( d^\beta - d^n \right) d^\gamma - \frac{1}{2} d^\gamma \left( \Sigma + \sigma^\beta \right) : \mathbb{S} : \left( \Sigma + \sigma^\beta \right) \right\rangle_Y,$$

for any  $\left( \vec{\sigma}^\beta, \vec{d}^\beta \right), \left( \vec{\sigma}^\gamma, \vec{d}^\gamma \right) \in \mathbb{R}^{M_\sigma} \times \mathbb{R}^{M_d}$ , where we use the abbreviations

$$\sigma^\kappa = \sum_{i=1}^{M_\sigma} \sigma_i^\kappa s_i \quad \text{as well as} \quad d^\kappa = \sum_{a=1}^{M_d} d_a^\kappa \delta_a \quad \text{for} \quad \kappa \in \{\beta, \gamma\} \tag{3.15}$$

and the inner product

$$\left\langle \left( \vec{\sigma}^\beta, \vec{d}^\beta \right), \left( \vec{\sigma}^\gamma, \vec{d}^\gamma \right) \right\rangle_M = \left\langle \sum_{i,j=1}^{M_\sigma} \sigma_i^\beta \sigma_j^\gamma s_i : s_j + \sum_{a,b=1}^{M_d} d_a^\beta d_b^\gamma \delta_a \delta_b \right\rangle_Y \tag{3.16}$$

on the space  $\mathbb{R}^{M_\sigma} \times \mathbb{R}^{M_d}$ . The operator (3.14) is closely related to the mixed variational principle (3.11) and (3.12). Indeed,  $\mathcal{A}_M$  may be written in the form

$$\mathcal{A}_M \left( \vec{\sigma}, \vec{d} \right) = \left( -\frac{\partial S_M}{\partial \vec{\sigma}}, \frac{\partial S_M}{\partial \vec{d}} \right). \tag{3.17}$$

Thus, any saddle point  $\left( \vec{\sigma}, \vec{d} \right)$  of the mixed variational principle (3.11) which satisfies  $d > d_-$  is a root of the operator  $\mathcal{A}_M$ . Conversely, any root  $\left( \vec{\sigma}, \vec{d} \right)$  of the operator  $\mathcal{A}_M$  is a saddle point of the variational principle (3.11). Of course, the same holds with the gradient of the function  $S_M$  in place of the operator  $\mathcal{A}_M$ . However, the simple sign reversal (3.17) in the first component provides the operator  $\mathcal{A}_M$  with better properties. Indeed, with the abbreviations (3.15), the identity

$$\left\langle \mathcal{A}_M \left( \vec{\sigma}^\beta, \vec{d}^\beta \right) - \mathcal{A}_M \left( \vec{\sigma}^\gamma, \vec{d}^\gamma \right), \left( \vec{\sigma}^\beta, \vec{d}^\beta \right) - \left( \vec{\sigma}^\gamma, \vec{d}^\gamma \right) \right\rangle_M = \left\langle \frac{2 + d^\beta + d^\gamma}{2} \left( \sigma^\beta - \sigma^\gamma \right) : \mathbb{S} : \left( \sigma^\beta - \sigma^\gamma \right) + \frac{1}{\alpha \Delta N} \left( d^\beta - d^\gamma \right)^2 \right\rangle_Y \tag{3.18}$$

holds for any  $\left( \vec{\sigma}^\beta, \vec{d}^\beta \right), \left( \vec{\sigma}^\gamma, \vec{d}^\gamma \right) \in \mathbb{R}^{M_\sigma} \times \mathbb{R}^{M_d}$ . Suppose that the stiffness distribution  $\mathbb{C}$  is uniformly bounded from above and from below

$$c_- \varepsilon : \varepsilon \leq \varepsilon : \mathbb{C} (x) : \varepsilon \leq c_+ \varepsilon : \varepsilon, \quad x \in Y, \quad \varepsilon \in \text{Sym}(m), \tag{3.19}$$

with positive constants  $c_\pm$ , and let  $\alpha_+$  be an upper bound for  $\alpha$ . Then, under the condition  $d^\kappa \geq d_-$  for  $\kappa \in \{\beta, \gamma\}$ , the identity (3.18) implies the estimate

$$\left\langle \mathcal{A}_M \left( \vec{\sigma}^\beta, \vec{d}^\beta \right) - \mathcal{A}_M \left( \vec{\sigma}^\gamma, \vec{d}^\gamma \right), \left( \vec{\sigma}^\beta, \vec{d}^\beta \right) - \left( \vec{\sigma}^\gamma, \vec{d}^\gamma \right) \right\rangle_M \geq c_- \left( 1 + d_- \right) \left\langle \left( \sigma^\beta - \sigma^\gamma \right) : \left( \sigma^\beta - \sigma^\gamma \right) \right\rangle_Y + \frac{1}{\Delta N \alpha_+} \left\langle \left( d^\beta - d^\gamma \right)^2 \right\rangle_Y. \tag{3.20}$$

In particular, as  $d_- > -1$ , the operator  $\mathcal{A}_M$  is strongly monotone, and the monotonicity constant does not depend on the chosen bases. We refer to Appendix B for a derivation of the identity (3.18). By similar arguments, the identity

$$\left\langle \mathcal{A}_M \left( \vec{\sigma}, \vec{d} \right), \left( \vec{\sigma}, \vec{d} \right) \right\rangle_M = \left\langle \frac{1 + d}{2} \left( \Sigma + \sigma \right) : \mathbb{S} : \sigma + \frac{1}{\alpha \Delta N} \left( d - d^n \right) d \right\rangle_Y, \tag{3.21}$$

using the abbreviations (3.15), may be deduced. Hence, the operator  $\mathcal{A}_M$  is also coercive. Moreover, due to its representation by a polynomial, the operator  $\mathcal{A}_M$  is continuous. Thus, as long as the constraint  $d \geq d_- > -1$  is satisfied, classical monotone operator theory [97] implies that there is a unique root of the operator  $\mathcal{A}_M$ .

For our computational experiments, it was not necessary to enforce the constraint  $d \geq d_-$  explicitly, see Section 4.3.1. Thus, the latter constraint may be regarded as a theoretical prerequisite that may not always be required in practice.

### 3.2. Implementation and solution of the discretized system

The proposed fatigue model permits a straightforward model-order reduction. Thus, precomputations on the microscale can be completed once and for all in an offline phase. The derivation of macroscopic equations and system matrices from the POD modes are discussed in this section.

The polynomial character of the saddle point functional (3.12) permits this saddle point functional, considered as a function of the mode coefficients, to be precomputed exactly (up to numerical precision). In particular, no access to the full fields is required during the online evaluation of the proposed multiscale fatigue-damage model. Let us first discuss why a polynomial potential enables a precomputation strategy. Suppose a function  $f$  of a vectorial variable  $\vec{z}$  is given. We assume the variable  $\vec{z}$  to be finite-dimensional with dimension  $M_z$ , and denote the components of  $\vec{z}$  by  $z_i$ , reserving Latin indices  $i, j, k$  for this purpose. Suppose furthermore that a number of modes  $\vec{z}^a$  ( $a = 1, \dots, M_m$ ) were selected, and we seek an approximation

$$\vec{z} = \sum_{a=1}^{M_m} \xi_a \vec{z}^a \tag{3.22}$$

in terms of suitable mode coefficients  $\xi_a$  ( $a = 1, \dots, M_m$ ). In particular, we are interested in the function

$$\tilde{f}(\xi_1, \dots, \xi_{M_m}) = f\left(\sum_{a=1}^{M_m} \xi_a \vec{z}^a\right), \tag{3.23}$$

which only depends on the mode coefficients. For MOR to be effective, the number of mode coefficients  $M_m$  in the representation (3.23) should be much smaller than the number of vector components  $M_z$ . For general functions  $f$ , little is gained by considering the function  $\tilde{f}$  (3.23), as its definition follows the indirect way via the variable  $\vec{z}$ . For polynomial functions  $f$ , in contrast, a different strategy can be followed. For concreteness, let us assume the function  $f$  to be a polynomial of degree 3, i.e., it may be expressed in the form

$$f(\vec{z}) = C + \sum_{i=1}^{M_z} f_i z_i + \sum_{i,j=1}^{M_z} f_{ij} z_i z_j + \sum_{i,j,k=1}^{M_z} f_{ijk} z_i z_j z_k \tag{3.24}$$

in terms of suitable coefficients  $C, f_i, f_{ij}$  and  $f_{ijk}$ . Then, inserting the mode representation (3.23), we obtain the expression

$$\tilde{f}(\xi_1, \dots, \xi_{M_m}) = C + \sum_{a=1}^{M_m} \tilde{f}_a \xi_a + \sum_{a,b=1}^{M_m} \tilde{f}_{ab} \xi_a \xi_b + \sum_{a,b,c=1}^{M_m} \tilde{f}_{abc} \xi_a \xi_b \xi_c, \tag{3.25}$$

which turns out to be a third-order polynomial in the *mode* coefficients and involves the precomputable coefficients

$$\begin{aligned} \tilde{f}_a &= \sum_{i=1}^{M_z} f_i z_i^a, \\ \tilde{f}_{ab} &= \sum_{i,j=1}^{M_z} f_{ij} z_i^a z_j^b, \\ \tilde{f}_{abc} &= \sum_{i,j,k=1}^{M_z} f_{ijk} z_i^a z_j^b z_k^c \end{aligned} \tag{3.26}$$

for  $a, b, c = 1, \dots, M_m$ .

Let us return to the fatigue-damage model at hand. For fixed modes (3.7) and (3.8), we set  $\vec{z} = (\vec{\sigma}, \vec{d})$ , i.e.,  $M_z = M_\sigma + M_d$ , and consider the objective function  $f = S_M$  (3.12), which is a third-order polynomial in the unknowns. Similar to the representation (3.25) involving the quantities (3.26), we obtain an expression of the

objective function  $S_M$  in the form

$$\begin{aligned}
 S_M(\vec{\sigma}, \vec{d}) = & -\frac{1}{2} \Sigma : \langle \mathbb{S} \rangle_Y : \Sigma - \Sigma : \Pi_i \sigma_i - \frac{1}{2} S_{ij} \sigma_i \sigma_j \\
 & - \frac{1}{2} \Sigma : \mathbb{D}_a : \Sigma d_a - \Sigma : \Lambda_{ia} \sigma_i d_a - \frac{1}{2} T_{ija} \sigma_i \sigma_j d_a \\
 & + \frac{1}{2\alpha \Delta \bar{N}} D_{ab} d_a d_b - \frac{1}{\alpha \Delta \bar{N}} D_{ab} d_a d_b^n + \frac{1}{2\alpha \Delta \bar{N}} D_{ab} d_a^n d_b^n.
 \end{aligned} \tag{3.27}$$

From Eq. (3.27) onwards, we use Einstein’s summation convention, i.e., we sum over pairs of appearing indices. For clarity, we reserve the indices  $a$  and  $b$  for damage modes, i.e., they sum from one to  $M_d$ , and use  $i$  as well as  $j$  for the stress modes, summing from one to  $M_\sigma$ . In the expression (3.27), the following quantities are precomputed:

$$\begin{aligned}
 \Pi_i &= \langle \mathbb{S} : s_i \rangle_Y, \\
 S_{ij} &= \langle s_i : \mathbb{S} : s_j \rangle_Y, \\
 \mathbb{D}_a &= \langle \delta_a \mathbb{S} \rangle_Y, \\
 \Lambda_{ia} &= \langle \delta_a \mathbb{S} : s_i \rangle_Y, \\
 T_{ija} &= \langle \delta_a s_i : \mathbb{S} : s_j \rangle_Y, \\
 D_{ab} &= \langle \delta_a \delta_b \rangle_Y,
 \end{aligned} \tag{3.28}$$

where the appearing indices have the same range as above. Notice also that all appearing quantities in (3.28) are symmetric in the index pairs  $(a, b)$  and  $(i, j)$ , respectively. To increase notational clarity, we use a Greek letter for  $\text{Sym}(m)$ -valued objects, Roman letters for scalar-valued objects and double stroke letters for fourth order tensor objects. The memory consumption for precomputing the quantities (3.28) is  $O(M_d M_\sigma^2)$ . As already mentioned in Section 3.1, the evolution equations of the proposed damage model (3.2), (3.3) are jointly quadratic in the internal variables. For a Galerkin-discretization using constant POD-modes the highest complexity in the precomputed matrices is thus in the order of three. Here, for  $M_d = O(M_\sigma)$ , the array  $T_{ija}$  has the highest complexity with  $M_d \times M_\sigma (M_\sigma + 1) / 2$  independent components.

Saddle points of the function  $S_M$  (3.27) satisfy the balance of linear momentum

$$S_{ij} \sigma_j + \Sigma : \Lambda_{ia} d_a + T_{ija} \sigma_j d_a = -\Sigma : \Pi_i \quad (i = 1, \dots, M_\sigma) \tag{3.29}$$

and Biot’s equation

$$\frac{1}{\alpha \Delta \bar{N}} D_{ab} d_b - \frac{1}{\alpha \Delta \bar{N}} D_{ab} d_b^n = \frac{1}{2} \Sigma : \mathbb{D}_a : \Sigma + \Sigma : \Lambda_{ia} \sigma_i + \frac{1}{2} T_{ija} \sigma_i \sigma_j \quad (a = 1, \dots, M_d). \tag{3.30}$$

Please notice that, if the macroscopic strain  $\bar{\epsilon}$  is specified instead of the macroscopic stress  $\Sigma$ , the equation

$$\langle \mathbb{S} \rangle_Y : \Sigma + \Pi_i \sigma_i + \mathbb{D}_a : \Sigma d_a + \Lambda_{ia} \sigma_i d_a = \bar{\epsilon} \tag{3.31}$$

needs to be added to the system in order to determine  $\Sigma$ .

For the convenience of the reader, an overview of offline and online computation is given in Fig. 6: Based on the fiber orientation interpolation concept [68], a finite number of fiber orientations is chosen. For each of these orientations, a short-fiber microstructure is generated [96]. For specified material parameters of matrix and fiber, the fatigue-damage evolution is computed using an FFT-based solver and a number of load cases, see Section 4.1 for details. Using the resulting solution fields, stress and damage modes are extracted via proper orthogonal decomposition (POD). More precisely, the damage and stress full-field solutions for all precomputed load cases and either all or a subset of cycle steps (see Section 4.3.2 for a study) are stored on disk. For a microstructure with  $N^3$  voxels, this amounts to storing  $N^3$  or  $6 \times N^3$  double-precision floating-point numbers per (damage or stress) snapshot, corresponding to either one or six scalars per voxel. Then, the POD correlation matrices are set up based on the  $L^2$  inner product both for the fatigue-damage variable and the stress field, and the damage and stress modes are extracted by the usual eigenvalue thresholding [98,99], see Section 4.3 for a study. Eventually, the relevant system matrices (as discussed in this section) are precomputed, and the model is ready for application on the component scale.

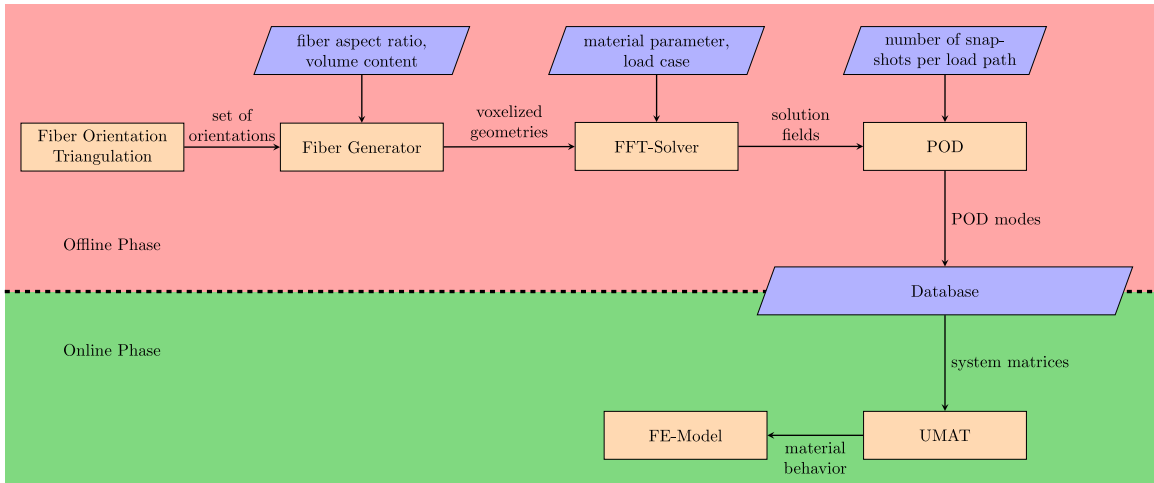


Fig. 6. Concept of precomputations and online phase.

Table 2  
Properties of the generated microstructures and the spatial discretization.

Parameter	Value	Unit
Fiber length	250	μm
Fiber diameter	10	μm
Aspect ratio	25	–
Fiber-volume content	17.8	%
Minimum fiber distance	5	μm
Average voxels per diameter	6.4	–
Cell length/fiber length	2.4	–

For solving Eqs. (3.29), (3.30) and (3.31), we use Newton’s method with backtracking. For strongly monotone operators, the latter scheme converges quadratically. As the termination condition for the scheme, we use

$$\|\nabla S\| \stackrel{!}{\leq} 10^{-8} \|\bar{\varepsilon}\|, \tag{3.32}$$

where we chose the Frobenius norm for the strain-amplitude tensor.

## 4. Computational investigations

### 4.1. Setup

The multiscale fatigue model described in Section 2.2 is discretized in time via an implicit Euler scheme and on a staggered grid in space [100]. For resolving the balance of linear momentum, we rely upon a nonlinear conjugate gradient method [101] to reduce the strain-based residual suggested in Kabel et al. [102] below a tolerance of  $10^{-5}$ .

The material model was implemented as a user subroutine in the FFT-based software FeelMath [103] and in Julia [104], which also served as the environment for the model-order reduction. For the computations, a Linux cluster equipped with Intel Xeon Gold 1648 processors was used.

### 4.2. Microscale studies

To study the material behavior on the microscale, we introduce three reference structures with different fiber orientations: an isotropic structure, a planar-isotropic structure and a unidirectional structure. The structures were generated by the sequential addition and migration algorithm (SAM) [96] using the parameters listed in Table 2.

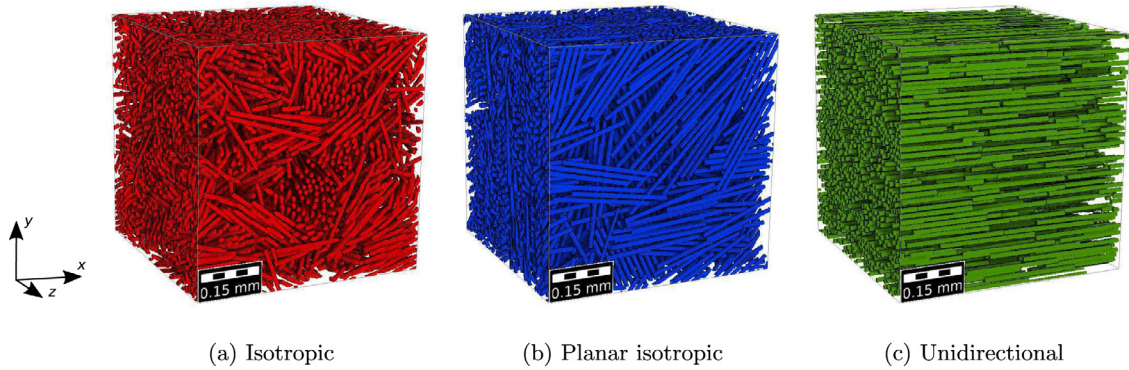


Fig. 7. Reference microstructures with different fiber orientations.

The resulting reference structures are shown in Fig. 7, visualized with GeoDict.<sup>1</sup> The SAM algorithm permits achieving high accuracy for the second-order fiber-orientation tensors. For example, for the isotropic and the planar isotropic microstructures shown in Fig. 7, the realized second-order fiber-orientation tensors read

$$A_{\text{iso}}^{(2)} = \begin{bmatrix} 0.333334 & -9.65272 \times 10^{-8} & 4.43788 \times 10^{-7} \\ -9.65272 \times 10^{-8} & 0.333333 & 2.71964 \times 10^{-8} \\ 4.43788 \times 10^{-7} & 2.71964 \times 10^{-8} & 0.333333 \end{bmatrix} \quad (4.1)$$

and

$$A_{\text{piso}}^{(2)} = \begin{bmatrix} 0.499739 & -0.000526419 & -4.66944 \times 10^{-6} \\ -0.000526419 & 0.499739 & 7.31379 \times 10^{-6} \\ -4.66944 \times 10^{-6} & 7.31379 \times 10^{-6} & 0.000521332 \end{bmatrix}, \quad (4.2)$$

respectively.

#### 4.2.1. On the necessary spatial resolution

For a start, we investigate the resolution that is necessary to obtain mesh-insensitive results. As our reference, we use 6.4 voxels per fiber diameter to resolve a fiber and call the respective voxel size  $h$ , see Table 2. Subsequently, we increase and decrease the resolution by a factor of two and compare the effective properties obtained from simulations on these structures to simulations on the reference structure. In Fig. 8, the evolution of the effective Young’s moduli [105] for the selected fiber orientations under uni-axial extension in  $x$ - and  $z$ -direction are shown. Due to the direction independence of the isotropic microstructure, only extension in  $x$ -direction is considered. For all three fiber orientations, the effective Young’s moduli are plotted in  $x$ - and  $z$ -direction.

We introduce the error measure

$$e^{\text{Young}} = 2 \max_i \frac{\|E_1(\bar{N}_i) - E_2(\bar{N}_i)\|}{\|E_1(\bar{N}_i) + E_2(\bar{N}_i)\|} \quad (4.3)$$

to quantify the deviation between two Young’s modulus evolutions  $E_1$  and  $E_2$ . For the isotropic structure, the deviation between the  $2 \times h$ -discretization and the  $0.5 \times h$ -discretization is 1.01% in  $x$ -direction and 1.21% in  $z$ -direction in terms of the stiffness-based error measure (4.3). Comparing the  $h$ -discretization and the  $0.5 \times h$ -discretization, the errors are below 0.5%, i.e., 0.25% in  $x$ -direction and 0.32% in  $z$ -direction.

For the planar-isotropic orientation, the observations are similar. For the unidirectional structure, the deviations at the  $2 \times h$  discretization are even less pronounced. Indeed, the unidirectional microstructure under loading in  $x$ -direction shows an error of 0.20% in  $x$ -direction and 0.01% in  $z$ -direction, when comparing the  $2 \times h$  discretization to the  $0.5 \times h$  discretization in terms of the stiffness-based error measure (4.3). Under loading in  $z$ -direction, the deviation is 0.20% in  $x$ -direction and 0.06% in  $z$ -direction.

<sup>1</sup> Math2Market GmbH, <http://www.geodict.de>.

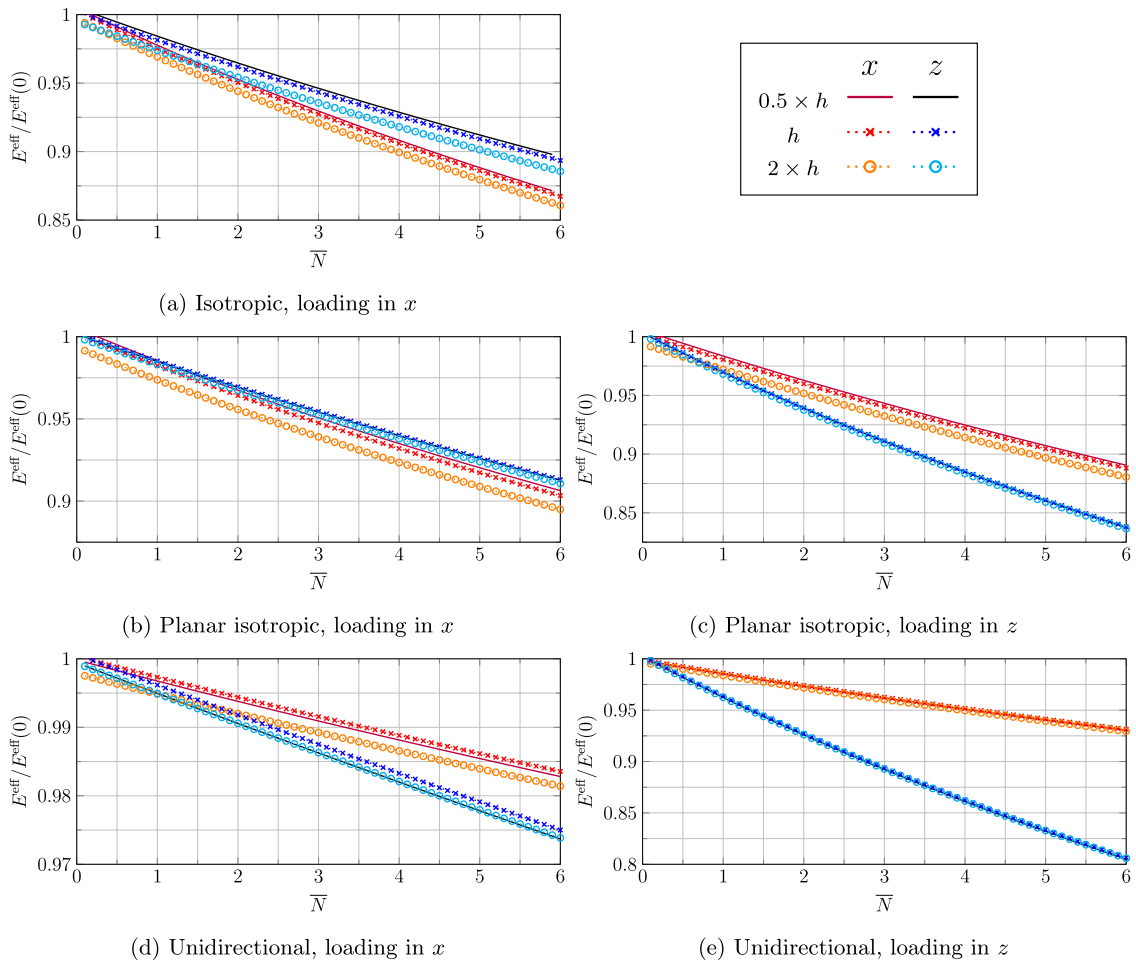


Fig. 8. Influence of the mesh size on the computational results.

Since the error measure (4.3) stays below 1% for all discussed load cases and directions, compared the  $h$ - to the  $2 \times h$ -discretization, we consider the deviation of the  $h$  discretization from the  $2 \times h$  discretization acceptable, and fix the mesh spacing to  $h$  for all subsequent studies.

4.2.2. On the necessary resolution in log-cycle space

As a second verification step on the microscale, we investigate the necessary step size  $\Delta \bar{N}$  in logarithmic cycle space. For an implicit Euler discretization with uniform step sizes  $\Delta \bar{N} \in \{0.05, 0.1, 0.2\}$ , results are shown in Fig. 9. Please notice that the logarithmic cycle variable  $\bar{N}$  is dimensionless.

The results show that the model turns out to be rather robust w.r.t. the chosen cycle step size. Even a step size of 0.2 produces only small errors. We fix a constant step size of 0.1 for the succeeding investigations.

4.2.3. On the necessary size of the unit cell

After studying the necessary resolution per fiber and the necessary step size, we turn our attention to the necessary size of the considered unit cell to produce representative results. Please keep in mind that the convexity of the model permits classical homogenization theory [92] to be applicable, see Section 2.2. In particular, the emergence of an effective material response on representative volume elements [70,106] is ensured, in contrast to the closely related model of Köbler et al. [64].

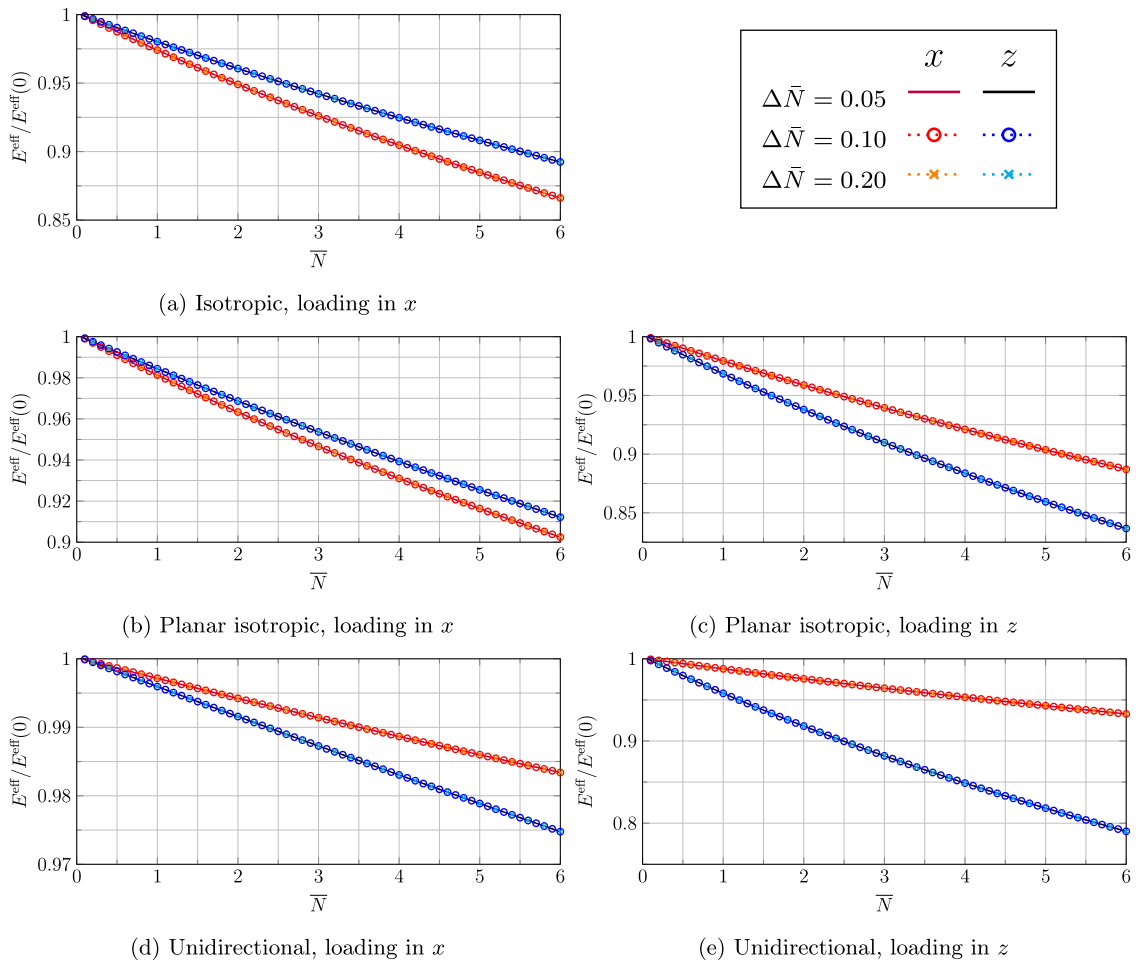


Fig. 9. Necessary resolution in logarithmic cycle space.

As our reference, we use volume elements with of  $384^3$  voxels, see Table 2. To study necessity and sufficiency of this fixed size, we increase and decrease the unit cell to comprise  $256^3$  and  $512^3$ -voxels, respectively. The arising edge length of the unit cells are 3.2 fiber lengths and 1.6 fiber lengths.

The evolving effective Young’s moduli are shown in Fig. 10, where we restrict to those cases with highest errors. We observe non-negligible deviations of the effective properties obtained from the 1.6 fiber length structures to those of the 3.2 fiber length structures for all considered loading scenarios. Comparing the Young’s modulus evolution of the  $256^3$ -voxel volume element to the  $512^3$ -voxel volume element, the stiffness-based error measure (4.3) is of the order of several percent for the considered load cases, with the highest error observed in the evolution of the Young’s modulus body of the planar-isotropic structure. For the planar-isotropic structure under loading in  $x$ -direction, the deviation reaches 3.0% in  $x$ -direction; for loading in  $z$ -direction, the deviation is 2.6% in  $x$ -direction. In particular, the volume element with  $256^3$  voxels fails to be representative.

Comparing the predictions for the  $384^3$ -structure, encompassing 2.4 fibers per edge, to the predictions of the larger volume size with  $512^3$  voxels and an edge length of 3.2 fiber lengths, these deviations decrease. For the isotropic and unidirectional structures, the errors of the Young’s modulus evolution under loading in  $x$ - and  $z$ -direction are smaller than 1.0%. The most critical case is the planar-isotropic structure under loading in  $x$ -direction. In this case, the deviation of the predicted Young’s modulus evolution in  $x$ -direction is 1%. This deviation is well within limits of engineering accuracy and we consider the  $384^3$  structure to be representative for the model at hand. For the remainder of the manuscript, we fix the size of the volume elements to be of an edge length of 2.4 fiber lengths.

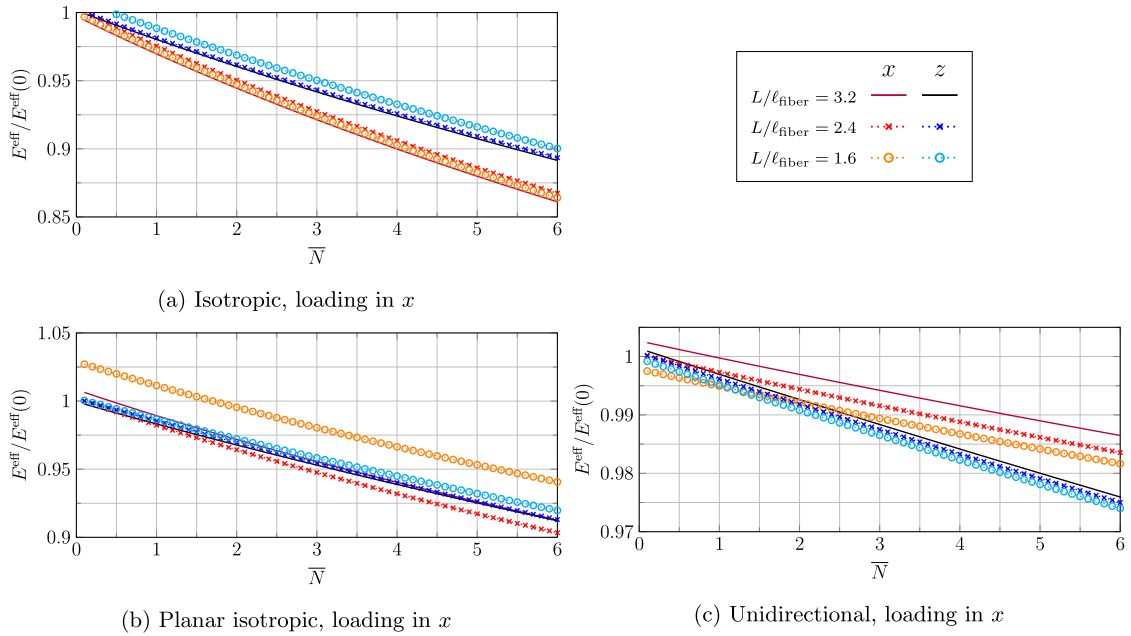


Fig. 10. Dependence of the computational results on the size of the unit cell.

#### 4.2.4. Fields on the microscale

To gain some understanding of the local fields on the microscale, we discuss the evolution of the damage and the strain field for the isotropic case under loading in  $x$ -direction. We load the structure shown in Fig. 7(b) at a constant stress amplitude of  $\sigma_{\max} = 100$  MPa.

The resulting damage and maximum principal strain fields in the  $x$ - $y$ -plane are shown in Fig. 11. Taking a look at the damage evolution, we observe that, in the early stages, damage is initiated at the fiber tips. Subsequently, the damage spreads through the structure. At the last cycle shown in Fig. 11(c), damage evolved also close to fibers which are oriented perpendicular to the loading direction. The maximum reduction of the stiffness locally reached for the isotropic structure under a load amplitude of 100 MPa in  $x$ -direction is 33%. This corresponds to a damage value of  $d = 0.5$ . The loss of the homogenized Young's modulus of the complete RVE in load direction at this time step is 10% and thus well in the order of typical stiffness loss in short fiber reinforced polymers prior to failure [31]. Higher loading amplitudes lead to more pronounced damage.

The strain evolution, starting from cycle  $N = 10$  ( $\bar{N} = 1$ ) up to cycle  $N = 10^7$  ( $\bar{N} = 7$ ), is shown in the bottom row in terms of the maximum principal strain. The evolution of the strain closely corresponds to the damage field evolution. In particular, it does not show localization. As for the damage field, the strain increases mainly at the tips of fibers oriented in loading direction. However, there are no microcrack-like patterns evolving throughout the matrix. Rather, the damage effects only lead to increasingly large strains at these critical spots.

#### 4.3. Reduced-order model

We investigate the capability of the reduced model to approximate the full-field solution in this section. For the sake of brevity, we use the isotropic, the planar isotropic and the unidirectional structure, shown in Fig. 7, for these studies. For each of the structures, we precomputed the load cases listed in Table 3. For assessing the accuracy of the reduced-order models, a strain-based error measure is introduced. For our stress driven simulations, the predicted effective (peak) strains of the full-field simulation  $\bar{\epsilon}_{\max}$  and the reduced-order model  $\bar{\epsilon}_{\max}^{\text{rom}}$  are compared in terms of the error measure

$$e^{\text{rom}} = \max_i \left( \frac{\|\bar{\epsilon}_{\max}(\bar{N}_i) - \bar{\epsilon}_{\max}^{\text{rom}}(\bar{N}_i)\|}{\|\bar{\epsilon}_{\max}(\bar{N}_i)\|} \right). \tag{4.4}$$

**Table 3**

Tensor components of the stress amplitude (in MPa) for precomputed load cases used for database generation.

load case	$\Sigma_{xx}^{\max}$	$\Sigma_{yy}^{\max}$	$\Sigma_{zz}^{\max}$	$\Sigma_{yz}^{\max}$	$\Sigma_{xz}^{\max}$	$\Sigma_{xy}^{\max}$
# 1	100 MPa	0	0	0	0	0
# 2	0	100 MPa	0	0	0	0
# 3	0	0	100 MPa	0	0	0
# 4	0	0	0	100 MPa	0	0
# 5	0	0	0	0	100 MPa	0
# 6	0	0	0	0	0	100 MPa

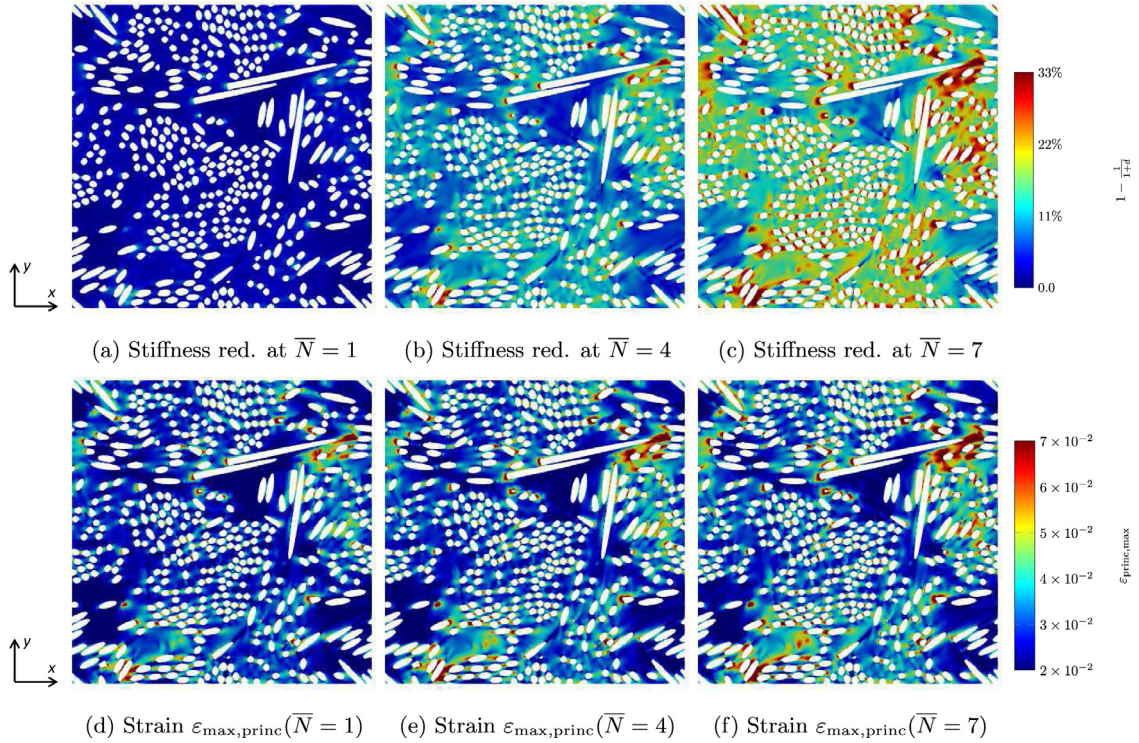


**Fig. 11.** Local stiffness reduction ( $1 - 1/(1 + d) \equiv d/(1 + d)$ , top) and maximum principal strain (bottom) on the isotropic structure under loading in  $x$ -direction.

#### 4.3.1. Mode selection

For selecting the modes of the reduced-order model, we investigated different strategies. In the end, the simplest strategy turned out to be the most powerful, and we shall report on it in the following.

Please recall that the continuous model discussed in Section 2.1 is uniquely solvable (upon implicit discretization in cycle space) and is characterized by a damage variable which can only grow point-wise. In the mixed formulation and upon a Galerkin discretization, see Section 3.1, these properties needed to be re-evaluated. It turned out that the mixed formulation is theoretically well-posed provided a lower bound  $d_-$  (strictly greater than  $d = -1$ ) is imposed on the damage field. Indeed, under this assumption, the operator whose roots correspond to solutions of the discretized equations turns out to be strongly monotone, and classical monotone-operator theory implies the claim.

For the study at hand, we use classical proper orthogonal decomposition (POD) for extracting damage and stress modes from the precomputed load cases. We chose the number of stress and damage modes to be identical, and refer to this number briefly as the number of modes.

Please note that working with the lower bound  $d_-$  is only sufficient for obtaining a well-posed model, and may be unnecessary in practice. Indeed, imposing such a constraint a priori may induce significant computational

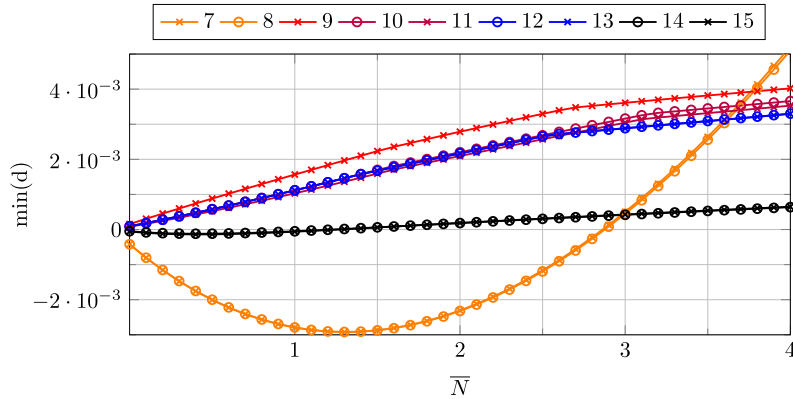


**Fig. 12.** Minimum value of the reconstructed damage field for the unidirectional structure under shear in the  $yz$ -plane for different numbers of incorporated modes  $M_\sigma$ .

overhead. Also, for our computational experiments, the reduced-order model could be solved rapidly and robustly even without additionally imposed constraints. The reasons behind this surprising behavior is studied more closely in the following. For this purpose, we reconstruct the damage fields predicted by the reduced-order model by summing the mode coefficients multiplied by their precomputed and stored damage modes at each step and extract the minimum damage-value from the corresponding full damage field.

The evolution of the minimum damage-value was computed for all load cases listed in Table 3. The most critical case in terms of the damage minimum for seven incorporated modes is the unidirectional structure under load case 4. The minimum damage-value evolution for this case is shown in Fig. 12 for different numbers of incorporated modes. For seven and eight modes, the minimum damage-value of the reconstructed damage field is  $d = -2.92 \times 10^{-3}$ . Albeit negative, this value is far from  $d = -1$ . By increasing the number of modes incorporated into the reduced-order model, the minimum damage-value increases. This does not come unexpected. Indeed, the reduced-order model approximates the full-field prediction with higher accuracy. The full-field prediction, on the other hand, satisfies the constraint  $d \geq 0$  by construction, see Section 2.1.

For 15 modes, the minimum damage-value is larger than  $d = -3.5 \times 10^{-4}$  for all load cases listed in Table 3 and all considered microstructures. Using 15 modes thus appears sufficient to inherit the well-posedness and stability properties from the continuous model. We continue with discussing the accuracy of the mode-selection procedure. In Fig. 13, the strain error (4.4) is shown vs. the number of incorporated modes for the isotropic, the planar isotropic and the unidirectional structure, respectively.

In general, the results of the reduced-order model agree well with the full-field predictions. Incorporating six modes into the reduced-order model already leads to a strain error below 1% for all load cases computed on the respective structures. Load cases with expected similar effective response, e.g., extension in  $x$ -direction,  $y$ -direction or  $z$ -direction for the isotropic structure (load cases 1, 2 and 3, respectively), show similar approximation behavior. This is remarkable, as we did not account for this symmetry explicitly in the mode-selection procedure.

We will use 15 POD-modes in the reduced-order model subsequently.

#### 4.3.2. Number of snapshots per path

To identify stress and damage modes, we use proper orthogonal decomposition. Some care has to be taken concerning the number of snapshots used for each considered loading path. We discuss the necessary choice for the number of snapshots per loading path (NSPL) in this section.

We use equidistant sampling steps in the logarithmic cycle variable  $\bar{N}$ . For the sake of brevity, we only discuss the planar-isotropic case here. The other fiber orientations lead to similar qualitative and quantitative results. The effect of including a different number of snapshots is shown in Fig. 14. We observe that the capability of the reduced-order model to approximate the effective strain amplitude predicted by the full-field model does not strongly depend on the chosen number of snapshots. Indeed, the strain-amplitude error (4.4) is in the same order of magnitude at all number of modes in Fig. 14 regardless of the number of snapshots (NSPL). Even a model order reduction based

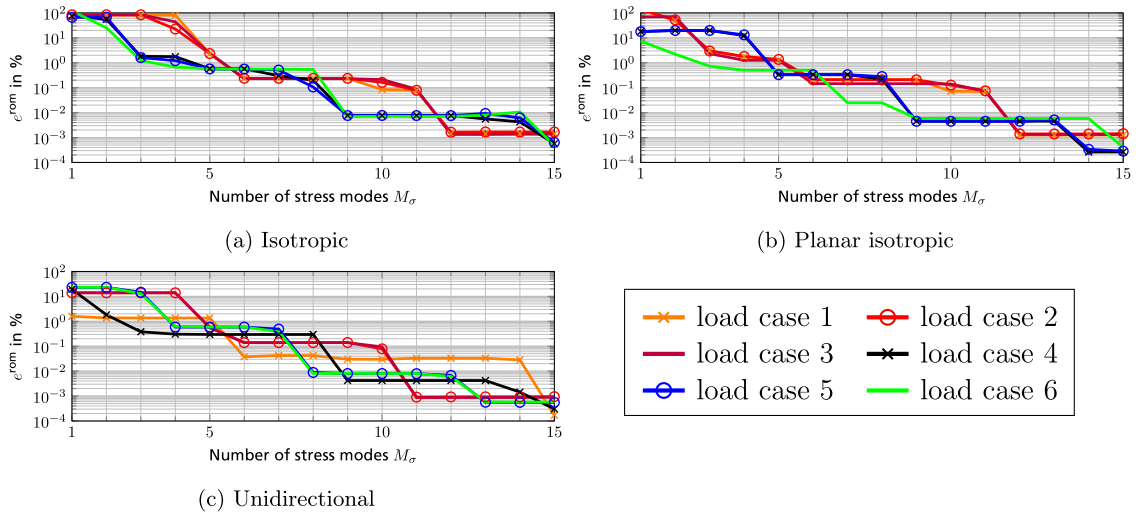


Fig. 13. Accuracy study for the database generated from ten snapshots per loading path.

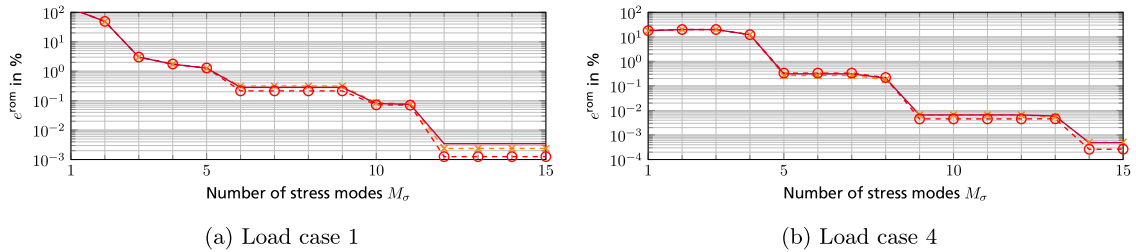


Fig. 14. Influence of the Number of Snapshots Per Loading path (NSPL) for the planar-isotropic structure (see Fig. 7(b))

on as few as three snapshots per load path appears to be reasonable. This appears to be a consequence of the non-localizing nature of the fatigue-damage model.

However, if the number of snapshots is chosen too small, the number of extractable modes is limited. On the other hand, the achieved approximation quality is certainly limited by choosing too few modes. Therefore, we fix NSPL= 10. An extension to more snapshots does not seem necessary and is thus omitted for the sake of faster precomputations.

#### 4.3.3. Necessary loading paths for database generation

In this section, we investigate the capabilities of the reduced-order model to predict the effective stiffness degradation for loading scenarios that were not accounted for in the database generation. More precisely, we discuss two variants: a change of the loading direction and a change of the loading amplitude. For the sake of brevity, we restrict to the planar-isotropic structure.

We start with the effect of changing the loading direction. We consider load cases of pure extension at the constant stress amplitude of  $\Sigma_{xx}^{\max} = 100$  MPa and stress ratio  $R = 0$ . The material parameters are chosen according to Table 1. First, we study loading in  $x$ -direction. Additionally we consider an extension at a  $45^\circ$  angle around the  $z$ -axis. Due to the symmetry of the planar-isotropic microstructure, both loading scenarios should give rise to identical responses (up to a rotation).

We consider a database built upon the load cases listed in Table 3, referred to as standard database in the following. Note that the first load case is part of the database. The *enriched* database comprises, in addition to the load cases of the standard database, the  $45^\circ$ -rotated full-field prediction.

The results of the reduced-order models for these two load cases, both, for the standard database and the enriched database, are plotted in Fig. 15. The Young’s modulus computed from the full-field prediction is referred to as  $E_{\text{full}}$

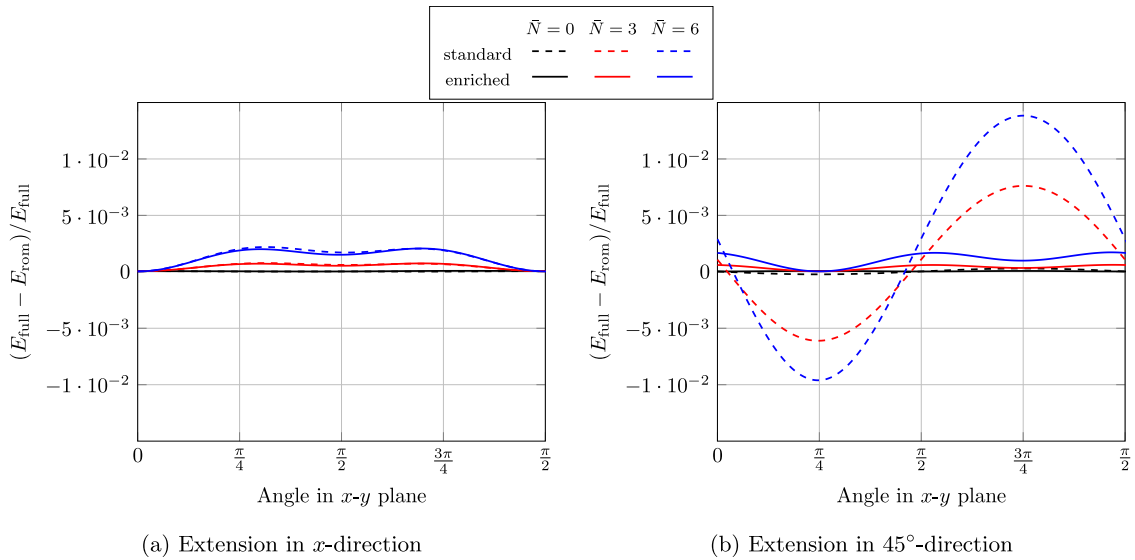


Fig. 15. Deviation of the direction-dependent Young’s modulus from the full-field prediction in the  $x$ – $y$ -plane for the planar-isotropic structure for different databases.

**Table 4**  
Strain-amplitude errors (4.4) for changing loading amplitude.

	Strain errors for loading in			
	$\Sigma_{xx}^{max}$	$\Sigma_{zz}^{max}$	$\Sigma_{yz}^{max}$	$\Sigma_{xy}^{max}$
20 MPa	$1.1 \times 10^{-5}$	$6.0 \times 10^{-6}$	$1.3 \times 10^{-6}$	$9.8 \times 10^{-7}$
100 MPa	$1.3 \times 10^{-5}$	$1.3 \times 10^{-5}$	$2.6 \times 10^{-6}$	$4.1 \times 10^{-6}$
500 MPa	$9.2 \times 10^{-2}$	$3.9 \times 10^{-2}$	$2.9 \times 10^{-3}$	$9.2 \times 10^{-2}$

and the Young’s modulus computed from the reduced-order model as  $E_{rom}$ . The error measure  $(E_{full} - E_{rom})/E_{full}$  is plotted over a range of  $180^\circ$  in the  $x$ – $y$ -plane, where  $0^\circ$  corresponds to the  $x$ -axis and  $90^\circ$  to the  $y$ -axis.

We observe that the first load case, extension in  $x$ -direction, leads to a negligible relative error of about 0.1%, both, for the standard and the enriched database. On the contrary, when considering the  $45^\circ$ -rotated load case, the standard database is not able to reproduce the load case with the same accuracy. At an angle of  $135^\circ$ , the Young’s modulus at  $\bar{N}$  predicted with the standard database deviates from the full-field prediction by a relative error of 1.4%. Yet, the induced error remains on an acceptable level.

When including the  $45^\circ$ -oriented extension load-case into the precomputations, the accuracy of the reduced-order model is increased. Both load cases, tension in  $x$ -direction and tension in  $45^\circ$  are predicted with similar accuracy in the order of 0.1%.

As a take-away message from these studies, we state that some caution has to be taken regarding a discretization of the space of possible loadings to select the modes from. Yet, the standard sampling with six load cases appears reasonable in terms of accuracy. To increase the accuracy, the sampling strategy could be extended in an adaptive way. For the work at hand, we fix the standard six load cases.

As a second step in studying the necessary precomputations, we investigate the effect of varying the loading amplitude. We restrict the computational examples to the planar-isotropic structure. Recall that precomputations with a peak stress  $\Sigma_{xx}^{max} = 100$  MPa are used to generate the database, see Table 3. For this study, we multiply these load amplitudes by factors of 5 and 0.2, respectively. Simulations at a peak stress of  $\Sigma_{xx}^{max} = 500$  MPa will exceed typical stress values in fatigue experiments and are only chosen here to test the capability of the numerical model to adapt to stress amplitudes higher than the training level. For the load cases with modified amplitudes, we compute the strain-amplitude error (4.4) by comparison of the full-field to the reduced-order model predictions. The results are shown in Table 4.

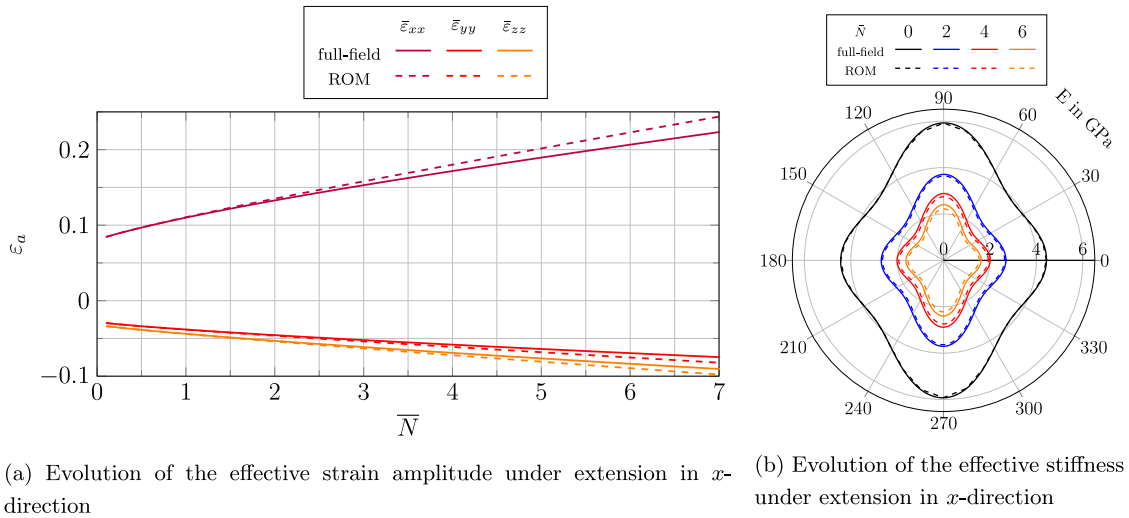


**Fig. 16.** Stiffness and strain results for planar-isotropic structure under 500 MPa loading: comparison of full-field predictions and reduced-order model.

**Table 5**

Strain-amplitude errors (4.4) for changing loading amplitude, trained at 20MPa.

	Strain errors for loading in			
	$\Sigma_{xx}^{\max}$	$\Sigma_{zz}^{\max}$	$\Sigma_{yz}^{\max}$	$\Sigma_{xy}^{\max}$
20 MPa	$2.9 \times 10^{-5}$	$3.5 \times 10^{-5}$	$4.1 \times 10^{-5}$	$4.2 \times 10^{-5}$
100 MPa	$1.4 \times 10^{-3}$	$6.3 \times 10^{-4}$	$7.1 \times 10^{-4}$	$2.0 \times 10^{-3}$
500 MPa	$1.1 \times 10^{-1}$	$6.2 \times 10^{-2}$	$8.6 \times 10^{-3}$	$2.4 \times 10^{-1}$

We observe that the load case with  $\Sigma_{xx}^{\max} = 20$  MPa, which is smaller than the training load case  $\Sigma_{xx}^{\max} = 100$  MPa included into the database, is predicted accurately with strain-amplitude errors below  $10^{-4}$ . For a higher amplitude at  $\Sigma^{\max} = 500$  MPa, the accuracy decreases significantly. We observe a maximum error of 9.23% in load cases 1 and 6. In Fig. 16(a), the strain amplitudes computed by the full-field model and the reduced-order model for this load case are shown in more detail. Up to strains of 0.13 in loading direction, the deviation of the full-field strain curve to the reduced-order model predictions is small. Indeed, at  $\bar{N} = 1.8$ , where the full-field model predicts  $\varepsilon_{a,xx} = 0.128$ , the reduced-order model predicts  $\varepsilon_{a,xx} = 0.130$ , which is a relative deviation of 1.6%. For further increasing strain amplitudes, the deviation between the effective strain-amplitude curve of the full-field model and of the reduced-order model increases, as well. In addition to the strain amplitude, we investigate the evolution of the Young's modulus body. For load case 1, the Young's modulus body in the  $x$ - $z$ -plane is plotted in Fig. 16(b). We observe that, even though the magnitude is not accurately met, the reduced-order model still predicts the shape of the Young's modulus body in accordance with the full-field solution, also at high cycle numbers.

Unexpectedly, despite being trained at 100 MPa, the database is most accurate for a stress amplitude of 20 MPa. To understand this effect more thoroughly, we trained a database with lower load amplitudes of 20 MPa and compare its accuracy to the standard database, trained at 100 MPa. We compare the errors produced by the 20 MPa database, see Table 5, to those of the standard database in Table 4. The most critical load case at an amplitude of 20 MPa can be reproduced with an accuracy of  $2.9 \times 10^{-5}$ , which has the same order of magnitude as the error produced by the 100-MPa database for the same load case of  $1.1 \times 10^{-5}$ . In contrast, the 100 MPa load cases treated by the 20-MPa database cannot be reproduced with the same accuracy as for the 100-MPa database. Indeed, the maximum error increases from  $1.3 \times 10^{-5}$  to  $2.0 \times 10^{-3}$ , which corresponds to a loss in accuracy by a factor of 154. The trend for even higher load amplitudes of 500 MPa is similar. This investigation reveals that the fatigue-damage evolution at lower stress amplitude is easier to approximate – as a result of the underlying physics – than at higher stress amplitudes. This is the reason for the higher accuracy of the 100 MPa database for a stress amplitude of 20 MPa.

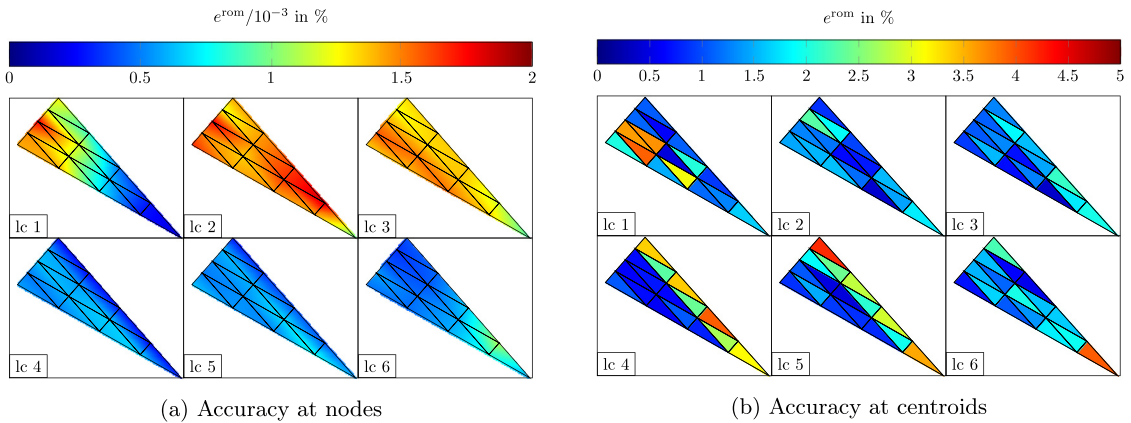


Fig. 17. Accuracy study on the fiber-orientation triangle: strain error (4.4) at precomputed and interpolated structures.

We conclude that the model may be safely used for computations where the strain evolution reaches strain levels of the training level or below, but some caution is advised when exceeding the pre-training levels. This effect is a consequence of the non-linearity of the model. It was with this insight at hand that we selected a training amplitude of 100 MPa, as the reasonable stress amplitudes of interest are covered in this way. Despite some deviations in the predicted effective strain amplitudes, the effective stiffness of the reduced-order model is predicted rather accurately.

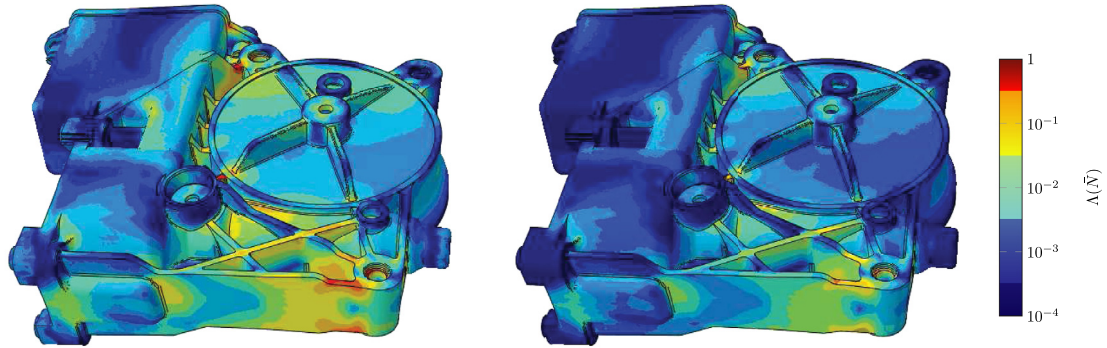
#### 4.3.4. Covering different fiber orientation states

With component-scale applications in mind, a variety of fiber-orientation states needs to be considered. Guided by the state of the art in injection-molding simulations [4], we consider a varying second-order fiber-orientation tensor [95] as the input for the generated microstructures. To create a database encompassing all possible second-order fiber-orientation tensors, we utilize the fiber-orientation interpolation procedure proposed by Köbler et al. [68]. Up to an orthogonal transformation, second-order fiber-orientation tensors may be parameterized by a two-dimensional triangle, corresponding to the two largest eigenvalues of the second-order fiber-orientation tensor. Based on a triangulation of this fiber-orientation triangle, a reduced-order model is identified for every node of this triangulation. Subsequently, the effective models are interpolated to the entire triangle. We refer to Köbler et al. [68] for details.

We discretize the fiber-orientation triangle by 15 nodes as shown in Fig. 17, resulting in 16 sub-triangles. For each of the 15 nodes, we generate microstructures and precompute all six load cases listed in Table 3 for these structures. These precomputations are then used to build a database via proper orthogonal decomposition, as described in Section 4.3. In a first verification step, we compare the evolution of the strain amplitude predicted by the full-field computations on these 15 structures with the predictions of the reduced-order model by means of the error measure (4.4). In Fig. 17(a), this error measure is plotted at each of the nodes for the reference load cases (lc), see Table 3. The accuracy on the precomputed structures is good for all microstructures and all considered load cases. The maximum observed strain-amplitude error is  $1.8 \times 10^{-4}$  for the structure with eigenvalues  $\lambda_1 = 0.417$ ,  $\lambda_2 = 0.417$  and  $\lambda_3 = 0.167$  under extension in  $x$ -direction (load case 1). We observe the errors in the extension load cases to be higher than the errors in the shear cases. The accuracy using 15 modes is sufficient for the precomputed structures. Note that the choice of 15 modes arises from the study on the non-negativity of the damage field, see Section 4.3.1. In terms of the accuracy choosing even fewer modes would be reasonable.

As a second verification step, we investigate the predictions of the model on fiber orientation states that have not been precomputed directly, but are interpolated from nearby precomputed states. For these structures within the faces of the discretized fiber-orientation triangle, as suggested by Köbler et al. [68], we compute the material response of the surrounding structures at the nodes of the discretized fiber-orientation triangle via the reduced-order model, and successively interpolate the effective stresses. This procedure increases the effort by a factor of three, both, in terms of CPU time and memory usage, as, for each Gauss point, three material laws have to be evaluated.

To assess the predictive capabilities of the interpolation procedure, we generated microstructures at the centroids of the 16 sub-triangles. The computed (full-field) effective strain-amplitude tensors serve as our reference. We



(a) Damage state for model in Köbler et al. [64]      (b) Damage state for model in work at hand

**Fig. 18.** Relative degradation of the acoustic tensor (5.1) after  $10^6$  cycles.

compare these effective strain amplitudes to the effective strain amplitudes predicted by the reduced-order model via interpolation in terms of the error measure (4.4). In Fig. 17(b), we observe that the strain errors do not exceed 5 % in the maximum strain-amplitude error. Since nodal errors are found to be very small, the latter error is mainly caused by the interpolation procedure. For the remainder of this work, we will use the presented fiber-orientation triangulation.

### 5. Component-scale simulations

We demonstrate the numerical capabilities of the presented model on component scale in terms of efficiency in both computational and memory usage by comparison to the recently published approach of Köbler et al. [64]. This models differs from the one presented in this work mainly in two aspects.

1. Non-local/local: The approach of Köbler et al. [64] introduces a damage-gradient term to avoid mesh-dependent results. The model proposed in this work is well-defined without an additional damage-gradient term.
2. Polynomial order: The highest polynomial order in the variables  $(\sigma, d)$  in Eqs. (3.2) and (3.3) is two, whereas the approach by Köbler et al. [64] leads to polynomials of the order of three in  $(\varepsilon, d)$ . Thus, less data needs to be processed at the Gauss point level for the former model.

In contrast to the approach presented in the work at hand, the model of Köbler et al. [64] permits localization, which makes the choice of the snapshots for proper orthogonal decomposition more difficult. Indeed, choosing an equidistant sampling method, Köbler et al. [64] incorporate 40 strain and 40 damage modes to reach acceptable accuracy. As discussed in Section 4.3, we make use of only 15 stress and 15 damage modes to ensure that the damage field is accurately captured.

We chose to demonstrate the efficiency of the model at hand on the same component and load case as described in Köbler et al. [64]: a short-fiber reinforced motor-housing subjected to fatigue loading. For details on the fiber-orientation distribution inside the component, as well as on the load case, we refer to Köbler et al. [64]. We use the simulation software ABAQUS [107] for computations on the macroscale. Both computations were performed on the same Linux cluster with 256 CPUs distributed on 16 nodes up to the cycle  $10^6$ .

Similar to Köbler et al. [64], we chose the determinant of the acoustic tensor  $A^{\text{aco}}$  as a quantitative measure for the material degradation and define

$$A(\bar{N}) = \max_{\|\mathbf{n}\|=1} \left[ 1 - \frac{\det A^{\text{aco}}(\mathbf{n}, \mathbf{C}(\bar{N}))}{\det A^{\text{aco}}(\mathbf{n}, \mathbf{C}(0))} \right], \tag{5.1}$$

where  $\mathbf{n}$  denotes a unit-normal vector, to assess the current damage state in the macroscopic model. The damage state of the motor housing component after  $10^6$  cycles is shown in Fig. 18 for, both, the quadratic type damage model of Köbler et al. [64] (Fig. 18(a)) and the compliance-based damage model proposed in the work at hand

**Table 6**  
Computational effort for the considered fatigue-damage models.

	CPU time	max. memory usage	av. memory usage
Quadratic damage model [64]	12200 h	65.5 GB	47.4 GB
Compliance based damage	712 h	39.0 GB	22.9 GB

(Fig. 18(b)). The regions of critical damage evolution, i.e., regions with a high relative decrease in the maximum of the acoustic tensor determinant, are found to be similar for both models.

The CPU time and the memory usage are shown in Table 6. Both, in terms of CPU time and memory usage, the efficiency of the model at hand is improved compared to the previous work. The CPU time of the compliance based damage model at hand leads to a speed up by a factor of 17 compared to the quadratic damage model [64]. The memory usage is on average improved by 52% and the peak memory usage by 40%.

This gain has three main causes. For a start, a lower number of incorporated modes is used, which decreases the size of the system matrices. Secondly, the polynomial in the damage evolution and stress–strain relationship in terms of the internal variables is of lower order. Thirdly, in contrast to Köbler et al. [64], we use a local model and do not have to incorporate gradient terms. The last two factors decrease the number of system matrices which need to be precomputed and stored.

## 6. Conclusions

We considered the problem of fatigue-damage evolution in short-fiber reinforced polymer composites. In order to account for the influence of the fiber reinforcements, both, in terms of the fiber geometry and the fiber orientation, we proposed a multiscale model for the fatigue-damage evolution in the stable second phase. The principal object of interest for us is the anisotropic stiffness degradation of such composites when subjected to (high-cycle) fatigue loading. Indeed, the failure behavior of thermoplastic components under fatigue loading appears to be difficult to predict if the stiffness decrease under fatigue loading previous to failure is not accounted for.

Motivated by the stability of the second phase in the fatigue-damage evolution, we explored the recently introduced class of damage models based on the compliance tensor [73]. Indeed, the inherent convexity of the model class appears sufficient for representing the fatigue-damage phenomena of interest, and offer to alleviate the computational burden associated to damage models with gradient extension [78].

We showed that, despite its simplicity, the model matches our experimental results rather well, provided the initial damage occurring in the first few cycles is taken into consideration. The precise value of the initial damage requires further studies.

With upscaling in mind, we studied a mixed formulation of the incremental potential of the multiscale fatigue-damage model. In this formulation, the potential is a third-order polynomial in the mode coefficients, and thus lends itself naturally to an efficient model-order reduction. Surprisingly, we could show that this mixed formulation inherits well-posedness from the purely primal formulation by rewriting the mixed formulation in terms of a specific operator, which is strongly monotone under a natural condition on the damage field.

The multiscale fatigue-damage model was tested thoroughly, both as a full-field and as a reduced-order model. Due to the (strongly) convex nature of the model, emergence of effective properties via suitable representative volume elements [106] is guaranteed. Also, due to the precluded localization, the multiscale model is characterized by high computational efficiency, which could be demonstrated on component scale.

This work was mainly concerned with setting up the multiscale technology necessary to handle industrial-scale applications. As a next step, it appears imperative to account for the initial damage caused in the first few cycles by an appropriate modification of the model and to investigate the extension to R-values different from zero as well as the dependence on the loading frequency. Supplemented by an appropriate failure criterion on the macroscopic scale, the presented multiscale fatigue-damage model will be ready for applications.

## Declaration of competing interest

The authors declare that they have no known competing financial interests or personal relationships that could have appeared to influence the work reported in this paper.

### Acknowledgments

MS acknowledges financial support of the German Research Foundation (DFG) within the International Research Training Group “Integrated engineering of continuous–discontinuous long fiber reinforced polymer structures” (GRK 2078).

We would like to thank Egon Moosbrugger for the experimental work. We are grateful to the anonymous reviewers, whose constructive remarks led to a significant improvement of the manuscript.

### Appendix A. Derivation of the saddle-point problem

We wish to establish the equivalence of minimizing the Ortiz–Stainier potential (2.20)

$$F(\bar{\varepsilon}, u, d) = \left\langle \frac{1}{2(1+d)} (\bar{\varepsilon} + \nabla^s u) : \mathbb{C} : (\bar{\varepsilon} + \nabla^s u) + \frac{1}{2\alpha\Delta\bar{N}} (d - d^n)^2 \right\rangle_Y - \bar{\varepsilon} : \Sigma \quad (\text{A.1})$$

and the variational principle (3.4)

$$S(\sigma, d) \equiv \left\langle -\frac{(1+d)}{2} \sigma : \mathbb{S} : \sigma + \frac{1}{2\alpha\Delta\bar{N}} (d - d^n)^2 \right\rangle_Y \longrightarrow \min_d \max_{\substack{\text{div } \sigma=0 \\ \langle \sigma \rangle_Y = \Sigma}} \quad (\text{A.2})$$

in terms of the relationship (3.2)

$$\varepsilon = (1+d) \mathbb{S} : \sigma. \quad (\text{A.3})$$

This appendix provides a derivation based on convex duality. More precisely, suppose a convex function  $f : X \rightarrow \mathbb{R}$  is given on a Banach space  $X$ . Let  $f^* : X' \rightarrow \mathbb{R}$  be its Legendre transform

$$f^*(y) = \sup_{x \in X} \langle x, y \rangle - f(x), \quad (\text{A.4})$$

where  $\langle \cdot, \cdot \rangle$  denotes the natural pairing  $\langle \cdot, \cdot \rangle : X \times X' \rightarrow \mathbb{R}$ . Suppose that a closed subspace  $U \subseteq X$  is given, and let  $U^* \subseteq X^*$  be its annihilator

$$U^* = \{y \in X^* \mid \langle y, x \rangle = 0 \text{ for all } x \in U\}. \quad (\text{A.5})$$

Then, according to convex duality [108, Thm. 31.4], the identity

$$\min_{x \in U} f(x) = - \min_{y \in U^*} f^*(y) \quad (\text{A.6})$$

holds. For the problem at hand, we consider the space  $X$  to consist of square-integrable strain (or stress) fields on the unit cell  $Y$ , and we consider the objective function

$$f(\varepsilon) = \left\langle \frac{1}{2(1+d)} \varepsilon : \mathbb{C} : \varepsilon + \frac{1}{2\alpha\Delta\bar{N}} (d - d^n)^2 \right\rangle_Y - \langle \varepsilon \rangle_Y : \Sigma, \quad (\text{A.7})$$

treating the damage variable  $d$  as a parameter, and work on the subspace of kinematically compatible strains

$$U = \{\varepsilon \in X \mid \varepsilon = \bar{\varepsilon} + \nabla^s u \text{ for some } \bar{\varepsilon} \text{ and } u\}. \quad (\text{A.8})$$

The Legendre transform of the function (A.7) computes as

$$f^*(\tau) = \left\langle \frac{(1+d)}{2} (\Sigma + \tau) : \mathbb{S} : (\Sigma + \tau) - \frac{1}{2\alpha\Delta\bar{N}} (d - d^n)^2 \right\rangle_Y \quad (\text{A.9})$$

in terms of the compliance  $\mathbb{S} = \mathbb{C}^{-1}$ . Indeed, the Legendre dual (A.4) is defined in terms of a maximization principle

$$f^*(\tau) = \sup_{\varepsilon \in X} \langle \tau : \varepsilon \rangle_Y - \left\langle \frac{1}{2} \varepsilon : \tilde{\mathbb{C}} : \varepsilon + \frac{1}{2\alpha\Delta\bar{N}} (d - d^n)^2 \right\rangle_Y + \langle \varepsilon \rangle_Y : \Sigma, \quad (\text{A.10})$$

whose critical points  $\varepsilon \in X$  satisfy

$$\tau - \tilde{\mathbb{C}} : \varepsilon + \Sigma = 0, \text{ i.e., } \varepsilon = \tilde{\mathbb{S}} : (\Sigma + \tau). \quad (\text{A.11})$$

Here, we set

$$\tilde{\mathbb{C}} = \frac{1}{1+d} \mathbb{C} \quad \text{and} \quad \tilde{\mathbb{S}} = (1+d)\mathbb{S} \tag{A.12}$$

for notational brevity. Inserting the explicit expression for the strain field  $\varepsilon$  into the definition (A.10) yields

$$\begin{aligned} f^*(\tau) &= \left\langle \tau : \tilde{\mathbb{S}} : (\Sigma + \tau) \right\rangle_Y - \left\langle \frac{1}{2} (\Sigma + \tau) : \tilde{\mathbb{S}} : (\Sigma + \tau) + \frac{1}{2\alpha\Delta\bar{N}} (d - d^n)^2 \right\rangle_Y + \left\langle \Sigma : \tilde{\mathbb{S}} : (\Sigma + \tau) \right\rangle_Y \\ &= \left\langle (\Sigma + \tau) : \tilde{\mathbb{S}} : (\Sigma + \tau) \right\rangle_Y - \left\langle \frac{1}{2} (\Sigma + \tau) : \tilde{\mathbb{S}} : (\Sigma + \tau) + \frac{1}{2\alpha\Delta\bar{N}} (d - d^n)^2 \right\rangle_Y \\ &= \left\langle \frac{1}{2} (\Sigma + \tau) : \tilde{\mathbb{S}} : (\Sigma + \tau) - \frac{1}{2\alpha\Delta\bar{N}} (d - d^n)^2 \right\rangle_Y, \end{aligned} \tag{A.13}$$

i.e., the representation (A.9) emerges. To complete the picture, we note that the orthogonal complement<sup>2</sup>  $U^*$  takes the form

$$U^* = \{ \tau \in X \mid \langle \tau \rangle_Y = 0 \text{ and } \operatorname{div} \tau = 0 \}, \tag{A.14}$$

i.e., it consists of equilibrium stress fluctuations. Combined with the expression (A.10), we conclude by convex duality (A.6) that we may transform

$$\begin{aligned} &\min_{\bar{\varepsilon}, u} \left\langle \frac{1}{2(1+d)} (\bar{\varepsilon} + \nabla^s u) : \mathbb{C} : (\bar{\varepsilon} + \nabla^s u) + \frac{1}{2\alpha\Delta\bar{N}} (d - d^n)^2 \right\rangle_Y - \bar{\varepsilon} : \Sigma \\ &= - \min_{\substack{\operatorname{div} \tau = 0 \\ (\tau)_Y = 0}} \left\langle \frac{(1+d)}{2} (\Sigma + \tau) : \mathbb{S} : (\Sigma + \tau) - \frac{1}{2\alpha\Delta\bar{N}} (d - d^n)^2 \right\rangle_Y \\ &= - \min_{\substack{\operatorname{div} \sigma = 0 \\ (\sigma)_Y = \Sigma}} \left\langle \frac{(1+d)}{2} \sigma : \mathbb{S} : \sigma - \frac{1}{2\alpha\Delta\bar{N}} (d - d^n)^2 \right\rangle_Y \\ &= \max_{\substack{\operatorname{div} \sigma = 0 \\ (\sigma)_Y = \Sigma}} \left\langle -\frac{(1+d)}{2} \sigma : \mathbb{S} : \sigma + \frac{1}{2\alpha\Delta\bar{N}} (d - d^n)^2 \right\rangle_Y, \end{aligned} \tag{A.15}$$

where we introduced the total stress field  $\sigma = \Sigma + \tau$ . Moreover, the identification (A.11) turns into

$$\varepsilon = (1+d)\mathbb{S} : \sigma. \tag{A.16}$$

Last but not least, we further minimize over the damage field to conclude

$$\begin{aligned} &\min_{\bar{\varepsilon}, u, d} \left\langle \frac{1}{2(1+d)} (\bar{\varepsilon} + \nabla^s u) : \mathbb{C} : (\bar{\varepsilon} + \nabla^s u) + \frac{1}{2\alpha\Delta\bar{N}} (d - d^n)^2 \right\rangle_Y - \bar{\varepsilon} : \Sigma \\ &= \min_d \max_{\substack{\operatorname{div} \sigma = 0 \\ (\sigma)_Y = \Sigma}} \left\langle -\frac{(1+d)}{2} \sigma : \mathbb{S} : \sigma + \frac{1}{2\alpha\Delta\bar{N}} (d - d^n)^2 \right\rangle_Y, \end{aligned} \tag{A.17}$$

what was to be shown.

### Appendix B. Monotonicity of the operator $\mathcal{A}_M$

In this appendix, we wish to derive the identity (3.18)

$$\begin{aligned} &\left\langle \mathcal{A}_M(\bar{\sigma}^\beta, \bar{d}^\beta) - \mathcal{A}_M(\bar{\sigma}^\gamma, \bar{d}^\gamma), (\bar{\sigma}^\beta, \bar{d}^\beta) - (\bar{\sigma}^\gamma, \bar{d}^\gamma) \right\rangle_M \\ &= \left\langle \frac{2 + d^\beta + d^\gamma}{2} (\sigma^\beta - \sigma^\gamma) : \mathbb{S} : (\sigma^\beta - \sigma^\gamma) + \frac{1}{\alpha\Delta\bar{N}} (d^\beta - d^\gamma)^2 \right\rangle_Y. \end{aligned} \tag{B.1}$$

For fixed compliance tensor  $\mathbb{S}$  and  $d^n, \bar{\alpha} \in \mathbb{R}$ , we investigate the operator

$$\mathcal{A} : \operatorname{Sym}(m) \times \mathbb{R} \rightarrow \operatorname{Sym}(m) \times \mathbb{R}, \quad (\sigma, d) \mapsto \left( (1+d)\mathbb{S} : \sigma, \bar{\alpha}^{-1}(d - d^n) - \frac{1}{2}\sigma : \mathbb{S} : \sigma \right) \tag{B.2}$$

<sup>2</sup> As we are working in a Hilbert space, we may canonically identify the dual space with the primal Hilbert space, and exchange the annihilator by the orthogonal complement, both in view of Riesz' representation theorem.

For any  $(\sigma^\beta, d^\beta), (\sigma^\gamma, d^\gamma) \in \text{Sym}(m) \times \mathbb{R}_{\geq 0}$ , we observe

$$\begin{aligned} [\mathcal{A}(\sigma^\beta, d^\beta) - \mathcal{A}(\sigma^\gamma, d^\gamma)](\sigma^\beta - \sigma^\gamma, d^\beta - d^\gamma) &= [(1 + d^\beta)\mathbb{S} : \sigma^\beta - (1 + d^\gamma)\mathbb{S} : \sigma^\gamma] : (\sigma^\beta - \sigma^\gamma) \\ &\quad + \bar{\alpha}^{-1}(d^\beta - d^\gamma)^2 - \frac{1}{2}(\sigma^\beta : \mathbb{S} : \sigma^\beta - \sigma^\gamma : \mathbb{S} : \sigma^\gamma)(d^\beta - d^\gamma). \end{aligned} \tag{B.3}$$

Introducing the short-hand notation  $\tilde{d}^\kappa = 1 + d^\kappa, \kappa \in \{\beta, \gamma\}$ , we transform

$$\begin{aligned} & [\tilde{d}^\beta \mathbb{S} : \sigma^\beta - \tilde{d}^\gamma \mathbb{S} : \sigma^\gamma] : (\sigma^\beta - \sigma^\gamma) - \frac{1}{2}(\sigma^\beta : \mathbb{S} : \sigma^\beta - \sigma^\gamma : \mathbb{S} : \sigma^\gamma)(\tilde{d}^\beta - \tilde{d}^\gamma) \\ &= \tilde{d}^\beta \sigma^\beta : \mathbb{S} : \sigma^\beta - (\tilde{d}^\beta + \tilde{d}^\gamma) \sigma^\beta : \mathbb{S} : \sigma^\gamma + \tilde{d}^\gamma \sigma^\gamma : \mathbb{S} : \sigma^\gamma \\ &\quad - \frac{1}{2}(\tilde{d}^\beta \sigma^\beta : \mathbb{S} : \sigma^\beta - \tilde{d}^\beta \sigma^\gamma : \mathbb{S} : \sigma^\gamma - \tilde{d}^\gamma \sigma^\beta : \mathbb{S} : \sigma^\beta + \tilde{d}^\gamma \sigma^\gamma : \mathbb{S} : \sigma^\gamma) \\ &= \frac{1}{2} \tilde{d}^\beta \sigma^\beta : \mathbb{S} : \sigma^\beta - (\tilde{d}^\beta + \tilde{d}^\gamma) \sigma^\beta : \mathbb{S} : \sigma^\gamma + \frac{1}{2} \tilde{d}^\gamma \sigma^\gamma : \mathbb{S} : \sigma^\gamma + \frac{1}{2} (\tilde{d}^\beta \sigma^\gamma : \mathbb{S} : \sigma^\gamma + \tilde{d}^\gamma \sigma^\beta : \mathbb{S} : \sigma^\beta) \tag{B.4} \\ &= \frac{1}{2} (\tilde{d}^\beta + \tilde{d}^\gamma) (\sigma^\beta : \mathbb{S} : \sigma^\beta - 2 \sigma^\beta : \mathbb{S} : \sigma^\gamma + \sigma^\gamma : \mathbb{S} : \sigma^\gamma) \\ &= \frac{\tilde{d}^\beta + \tilde{d}^\gamma}{2} (\sigma^\beta - \sigma^\gamma) : \mathbb{S} : (\sigma^\beta - \sigma^\gamma). \end{aligned}$$

Inserting this result back into the original formula, we obtain

$$[\mathcal{A}(\sigma^\beta, d^\beta) - \mathcal{A}(\sigma^\gamma, d^\gamma)](\sigma^\beta - \sigma^\gamma, d^\beta - d^\gamma) = \frac{2 + d^\beta + d^\gamma}{2} (\sigma^\beta - \sigma^\gamma) : \mathbb{S} : (\sigma^\beta - \sigma^\gamma) + \bar{\alpha}^{-1}(d^\beta - d^\gamma)^2. \tag{B.5}$$

Regarding  $\mathbb{C}, \bar{\alpha} = \alpha \Delta \bar{N}$  and  $d^n$  as dependent on  $x \in Y$ , averaging the latter identity proves the formula (B.1), as claimed.

## References

- [1] Y. Lee, S. Lee, J. Youn, K. Chung, T. Kang, Characterization of fiber orientation in short fiber reinforced composites with an image processing technique, *Mater. Res. Innov.* 6 (2002) 65–72.
- [2] H. Shen, S. Nutt, D. Hull, Direct observation and measurement of fiber architecture in short fiber-polymer composite foam through micro-CT imaging, *Compos. Sci. Technol.* 64 (13) (2004) 2113–2120.
- [3] P.A. Hessman, T. Riedel, F. Welschinger, K. Hornberger, T. Böhlke, Microstructural analysis of short glass fiber reinforced thermoplastics based on x-ray micro-computed tomography, *Compos. Sci. Technol.* 183 (2019) 107752.
- [4] F. Wittemann, R. Maertens, L. Kärger, F. Henning, Injection molding simulation of short fiber reinforced thermosets with anisotropic and non-Newtonian flow behavior, *Composites A* 124 (2019) 105476.
- [5] M.J. Park, S.J. Park, Modeling and simulation of fiber orientation in injection molding polymer composites, *Math. Probl. Eng.* 2011 (2011).
- [6] S. Felder, N.A. Vu, S. Reese, J.-W. Simon, Experimental and numerical investigation of the material behavior of semi-crystalline polyamide 6, *Tech. Mech.* 40 (2019) 22–30.
- [7] S. Felder, N.A. Vu, S. Reese, J.-W. Simon, Modeling the effect of temperature and degree of crystallinity on the mechanical response of polyamide 6, *Mech. Mater.* 148 (2020) 103476.
- [8] S. Rabinowitz, P. Beardmore, Cyclic deformation and fracture of polymers, *J. Mater. Sci.* 9 (1974) 81–99.
- [9] E.J. Kramer, L.L. Berger, Fatigue failure mechanisms in polymers, *Adv. Polymer Sci.* 91/92 (1990).
- [10] J. Besson, C. Berdin, S. Bugat, R. Desmorat, F. Feyel, S. Forest, E. Lorentz, E. Maine, T. Pardoën, A. Pineau, B. Tanguy, *Local Approach to Fracture*, Presses de l'École des Mines, Paris, 2004.
- [11] A. Jain, W. van Paeppegem, I. Verpoest, S.V. Lomov, A statistical treatment of the loss of stiffness during cyclic loading for short fiber reinforced injection molded composites, *Composites B* 103 (2016) 40–50.
- [12] K.C. Dao, D.J. Dicken, Fatigue failure mechanisms in polymers, *Polym. Eng. Sci.* 27 (4) (1987) 271–276.
- [13] S.B. Sapozhnikov, A.A. Shabley, A.V. Ignatova, Predicting the kinetics of hysteretic self-heating of GFRPs under high-frequency cyclic loading, *Compos. Struct.* 226 (2019) 111214.
- [14] A. Schaaf, M. De Monte, E. Moosbrugger, M. Vormwald, M. Quaresimin, Life estimation methodology for short fiber reinforced polymers under thermo-mechanical loading in automotive applications, *Mater. Sci. Eng. Technol.* 46 (2015) 214–228.
- [15] V. Crupi, E. Giglielmino, G. Risitano, F. Tavilla, Experimental analyses of SFRP material under static and fatigue loading by means of thermographic and DIC techniques, *Composites B* 77 (2015) 268–277.
- [16] H. Rolland, N. Saintier, N. Lenoir, A. King, G. Robert, Fatigue mechanisms description in short glass fibre reinforced thermoplastic by microtomographic observations, *Proc. Struct. Integr.* 2 (2016) 301–308.

- [17] E. Belmonte, M. De Monte, C. Hoffmann, M. Quaresimin, Damage mechanisms in a short glass fiber reinforced polyamide under fatigue loading, *Int. J. Fatigue* 94 (1) (2017) 145–157.
- [18] M.F. Arif, N. Saintier, F. Meraghni, J. Fitoussi, Y. Chemisky, G. Robert, Multiscale fatigue damage characterization in short glass fiber reinforced polyamide 66, *Composites B* 61 (2014) 55–65.
- [19] N. Sato, T. Kurauchi, S. Sato, O. Kamigaito, Microfailure behaviour of randomly dispersed short fibre reinforced thermoplastic composites obtained by direct SEM observation, *J. Mater. Sci.* 26 (1991) 3891–3893.
- [20] H. Rolland, N. Saintier, I. Raphael, N. Lenoir, A. King, G. Robert, Fatigue damage mechanisms of short fiber reinforced PA66 as observed by in-situ synchrotron X-ray microtomography, *Composites B* 143 (2018) 217–229.
- [21] E. Chebbi, J. Mars, M. Wali, F. Dammak, Fatigue behavior of short glass fiber reinforced polyamide 66: Experimental study and fatigue damage modelling, *Period. Polytech. Mech. Eng.* 60 (4) (2016) 247–255.
- [22] L.G. Moretto Lise, Investigation of Damage Evolution Due to Cyclic Mechanical Loads and Load/frequency Spectra-Effects in Short-Fibre-Reinforced Thermoplastics (Ph.D. thesis), Universidad Federale De Santa Catarina, 2020.
- [23] H. Nouri, F. Meraghni, P. Lory, Fatigue damage model for injection-molded short glass fibre reinforced thermoplastics, *Int. J. Fatigue* 31 (2009) 934–942.
- [24] W. Van Paepegem, J. Degrieck, A new coupled approach of residual stiffness and strength for fatigue of fibre-reinforced composites, *Int. J. Fatigue* 24 (2002) 747–762.
- [25] P. Maimí, P.P. Camanho, J.A. Mayugo, C.G. Dávila, A continuum damage model for composite laminates: Part I – Constitutive model, *Mech. Mater.* 39 (2007) 897–908.
- [26] S.T. Pino, R. Darvizeh, P. Robinson, C. Schuecker, P.P. Camanho, Material and structural response of polymer-matrix fibre-reinforced composites, *J. Compos. Mater.* 46 (2012) 2313–2341.
- [27] K. Matouš, M.G. Geers, V.G. Kouznetsova, A. Gillman, A review of predictive nonlinear theories for multiscale modeling of heterogeneous materials, *J. Comput. Phys.* 330 (2017) 192–220.
- [28] B. Klusemann, H.J. Böhm, B. Svendsen, Homogenization methods for multi-phase elastic composites with non-elliptical reinforcements: Comparisons and benchmarks, *Eur. J. Mech. A Solids* 34 (2012) 21–37.
- [29] A. Krairi, I. Doghri, G. Robert, Multiscale high cycle fatigue models for neat and short fiber reinforced thermoplastic polymers, *Int. J. Fatigue* 92 (2016) 179–192.
- [30] S. Kammoun, I. Doghri, L. Brassart, L. Delannay, Micromechanical modeling of the progressive failure in short glass–fiber reinforced thermoplastics – First Pseudo-Grain Damage model, *Composites A* 73 (2015) 166–175.
- [31] A. Jain, J.M. Veas, S. Straesser, W. van Paepegem, I. Verpoest, S.V. Lomov, The Master SN curve approach – A hybrid multi-scale fatigue simulation of short fiber reinforced composites, *Composites A* 91 (2016) 510–518.
- [32] A. Jain, W. van Paepegem, I. Verpoest, S.V. Lomov, A feasibility study of the Master SN curve approach for short fiber reinforced composites, *Int. J. Fatigue* 91 (2016) 264–274.
- [33] G. Erhard, *Designing with Polymers*, Carl Hanser Publishing, Munich/Vienna, 1999.
- [34] C. Guster, G. Pinter, A. Mösenbacher, W. Eichseder, Evaluation of a simulation process for fatigue life calculation of short fibre reinforced plastic components, *Procedia Eng.* 10 (2011) 2104–2109.
- [35] A. Mösenbacher, J. Brunbauer, P.F. Pichler, C. Guster, G. Pinter, Modelling and validation of fatigue life calculation method for short fiber reinforced injection molded parts, in: 16th European Conference on Composite Materials, 2014, pp. 1–8.
- [36] A. Zago, G.S. Springer, Fatigue lives of short fiber reinforced thermoplastics parts, *J. Reinf. Plast. Compos.* 20 (2001) 606–620.
- [37] A. Bernasconi, P. Davoli, A. Basile, A. Filippi, Effect of fibre orientation on the fatigue behaviour of a short glass fibre reinforced polyamide-6, *Int. J. Fatigue* 29 (2007) 199–208.
- [38] M. De Monte, E. Moosbrugger, M. Quaresimin, Influence of temperature and thickness on the off-axis behaviour of short glass fibre reinforced polyamide 6.6 cyclic loading, *Composites A* 42 (10) (2010) 1368–1379.
- [39] B. Klimkeit, Y. Nadot, S. Castagnet, C. Nadot-Martin, C. Dumas, S. Bergamo, M. Sonsino, A. Büter, Multiaxial fatigue life assessment for reinforced polymers, *Int. J. Fatigue* 33 (2011) 766–780.
- [40] S. Mortazavian, A. Fatemi, Fatigue behavior and modeling of short fiber reinforced polymer composites including anisotropy and temperature effects, *Int. J. Fatigue* 77 (2015) 12–27.
- [41] F. Feyel, Multiscale FE2 elastoviscoplastic analysis of composite structures, *Comput. Mater. Sci.* 16 (1999) 344–354.
- [42] J. Fish, Q. Yu, Failure models and criteria for FRP under in-plane or three-dimensional stress states including shear non-linearity, *Compos. Sci. Technol.* 61 (2001) 2215–2222.
- [43] L. Tikarouchine, A. Benaarbia, G. Chatzigeorgia, F. Meraghni, Micromechanical modeling of the progressive failure in short glass–fiber reinforced thermoplastics – First Pseudo-Grain Damage model, *Compos. Struct.* 255 (2021) 112926.
- [44] H. Moulinec, P. Suquet, A numerical method for computing the overall response of nonlinear composites with complex microstructure, *Comput. Methods Appl. Mech. Engrg.* 157 (1998) 69–94.
- [45] J.C. Michel, H. Moulinec, P. Suquet, A computational scheme for linear and non-linear composites with arbitrary phase contrast, *Internat. J. Numer. Methods Engrg.* 52 (2001) 139–160.
- [46] J. Spahn, H. Andrä, M. Kabel, R. Müller, A multiscale approach for modeling progressive damage of composite materials using fast Fourier transforms, *Comput. Methods Appl. Mech. Engrg.* 268 (2014) 871–883.
- [47] J. Kochmann, S. Wulfinghoff, S. Reese, J.R. Mianroodi, B. Svendsen, Two-scale FE–FFT- and phase-field-based computational modeling of bulk microstructural evolution and macroscopic material behavior, *Comput. Methods Appl. Mech. Engrg.* 305 (2016) 89–110.
- [48] J. Kochmann, S. Wulfinghoff, L. Ehle, J. Mayer, B. Svendsen, S. Reese, Efficient and accurate two-scale FE–FFT-based prediction of the effective material behavior of elasto-viscoplastic polycrystals, *Comput. Mech.* 61 (2018) 751–764.

- [49] G.J. Dvorak, Transformation field analysis of inelastic composite materials, *Proc. Math. Phys. Sci.* 437 (1900) (1992) 311–327.
- [50] G.J. Dvorak, J. Zhang, Transformation field analysis of damage evolution in composite materials, *J. Mech. Phys. Solids* 49 (2001) 2517–2541.
- [51] J.C. Michel, P. Suquet, Nonuniform transformation field analysis, *Int. J. Solids Struct.* 40 (25) (2003) 6937–6955.
- [52] J.-C. Michel, P. Suquet, Nonuniform transformation field analysis: a reduced model for multiscale nonlinear problems in solid mechanics, *Multiscale Model. Solid Mech. - Comput. Approach.* (2009) 159–206.
- [53] F. Fritzen, M. Leuschner, Reduced basis hybrid computational homogenization based on a mixed incremental formulation, *Comput. Methods Appl. Mech. Engrg.* 260 (2013) 143–154.
- [54] Z. Liu, M.A. Bessa, W.K. Liu, Self-consistent clustering analysis: An efficient multi-scale scheme for inelastic heterogeneous materials, *Comput. Methods Appl. Mech. Engrg.* 306 (2016) 319–341.
- [55] S. Wulfinghoff, F. Cavaliere, S. Reese, Model order reduction of nonlinear homogenization problems using a Hashin-Shtrikman type finite element method, *Comput. Methods Appl. Mech. Engrg.* 330 (2018) 149–179.
- [56] M. Schneider, On the mathematical foundations of the self-consistent clustering analysis for non-linear materials at small strains, *Comput. Methods Appl. Mech. Engrg.* 354 (2019) 783–801.
- [57] T. Furukawa, Y. Genki, Implicit constitutive modelling for viscoplasticity using neural networks, *Internat. J. Numer. Methods Engrg.* 43 (1998) 195–219.
- [58] R. Haj-Ali, D.A. Pecknold, J. Ghaboussi, G.Z. Voyiadjis, Simulated micromechanical models using artificial neural networks, *J. Eng. Mech.* 127 (7) (2001) 730–738.
- [59] Z. Liu, C.T. Wu, M. Koishi, A deep material network for multiscale topology learning and accelerated nonlinear modeling of heterogeneous materials, *Comput. Methods Appl. Mech. Engrg.* 345 (2019) 1138–1168.
- [60] S. Gajek, M. Schneider, T. Böhlke, On the micromechanics of deep material networks, *J. Math. Phys. Solids* 142 (2020) 103984.
- [61] S. Gajek, M. Schneider, T. Böhlke, An FE-DMN method for the multiscale analysis of short fiber reinforced plastic components, *Comput. Methods Appl. Mech. Engrg.* 384 (2021) 113952.
- [62] Z. Liu, H. Wei, T. Huang, C.T. Wu, Intelligent multiscale simulation based on process-guided composite database, 2020, pp. 1–15, arxiv e-prints arXiv:2003.09491.
- [63] N. Mentges, B. Dashtbozorg, S.M. Mirkhalaf, A micromechanics-based artificial neural networks model for elastic properties of short fiber composites, *Composites B* 213 (2021) 108736.
- [64] J. Köbler, N. Magino, H. Andrä, F. Welschinger, R. Müller, M. Schneider, A computational multi-scale model for the stiffness degradation of short-fiber reinforced plastics subjected to fatigue loading, *Comput. Methods Appl. Mech. Engrg.* 373 (2021) 113522.
- [65] C. Miehe, M. Hofacker, F. Welschinger, A phase field model for rate-independent crack propagation: Robust algorithmic implementation based on operator splits, *Comput. Methods Appl. Mech. Engrg.* 199 (2010) 2765–2778.
- [66] C. Kuhn, R. Müller, A continuum phase field model for fracture, *Eng. Fract. Mech.* 77 (18) (2010) 3625–3634.
- [67] M. Ambati, T. Gerasimov, L. De Lorenzis, A review on phase-field models of brittle fracture and a new fast hybrid formulation, *Comput. Mech.* 55 (2015) 383–405.
- [68] J. Köbler, M. Schneider, F. Ospald, H. Andrä, R. Müller, Fiber orientation interpolation for the multiscale analysis of short fiber reinforced composite parts, *Comput. Mech.* 61 (2018) 729–750.
- [69] J.-C. Michel, P. Suquet, Effective potentials in nonlinear polycrystals and quadrature formulae, *Proc. R. Soc. Lond. Ser. A Math. Phys. Eng. Sci.* 473 (2017) 20170213.
- [70] I.M. Gitman, H. Askes, L. Sluys, Representative volume: Existence and size determination, *Eng. Fract. Mech.* 74 (2007) 2518–2534.
- [71] L.M. Kachanov, Time of the rupture process under creep conditions, *Izv. Akad. Nauk SSSR. Otd. Tekh. Nauk. Mekh. I Mashinostroenie* 8 (1958) 26–31.
- [72] J. Lemaitre, *A Course on Damage Mechanics*, Springer, Berlin Heidelberg, 1996.
- [73] J. Görthofer, M. Schneider, A. Hrymak, T. Böhlke, A convex anisotropic damage model based on the compliance tensor, *Int. J. Damage Mech.* (2020) 1–44, Online.
- [74] S. Govindjee, Anisotropic modelling and numerical simulation of brittle damage in concrete, *Internat. J. Numer. Methods Engrg.* 38 (1995) 3611–3633.
- [75] S. Wulfinghoff, M. Fassin, S. Reese, A damage growth criterion for anisotropic damage models motivated from micromechanics, *Int. J. Solids Struct.* 121 (2017) 21–32.
- [76] R. Vignjevic, N. Djordjevic, T. De Vuyst, S. Gemkow, Modelling of strain softening materials based on equivalent damage force, *Comput. Methods Appl. Mech. Engrg.* 335 (2018) 52–68.
- [77] J. Lemaitre, A continuous damage mechanics model for ductile fracture, *J. Eng. Mater. Technol.* 107 (1) (1985) 83–89.
- [78] R.H.J. Peerlings, W.A. Brekelmans, R. de Borst, M.G.H. Geers, Gradient-enhanced damage modelling of high-cycle fatigue, *Internat. J. Numer. Methods Engrg.* 49 (2000) 1547–1569.
- [79] S. Forest, E. Lorentz, *Localization phenomena and regularization methods*, Les Presses de L’Ecole Des Mines de Paris (2004) 311–317.
- [80] A. Mielke, T. Roubicek, J. Zeman, Complete damage in elastic and viscoelastic media and its energetics, *Comput. Methods Appl. Mech. Engrg.* 199 (2010) 1242–1253.
- [81] B. Bourdin, G.A. Francfort, J.-J. Margio, The variational approach to fracture, *J. Elasticity* 91 (2008) 5–148.
- [82] C. Miehe, F. Welschinger, M. Hofacker, Thermodynamically consistent phase-field models of fracture: Variational principles and multi-field FE implementations, *Internat. J. Numer. Methods Engrg.* 83 (10) (2010) 1273–1311.
- [83] P. Carrara, M. Ambati, R. Alessi, L. De Lorenzis, A framework to model the fatigue behavior of brittle materials based on a variational phase-field approach, *Comput. Methods Appl. Mech. Engrg.* 361 (2020) 112731.
- [84] J.-C. Michel, P. Suquet, A model-reduction approach in micromechanics of materials preserving the variational structure of constitutive relations, *J. Mech. Phys. Solids* 90 (2016) 254–285.

- [85] J.-C. Michel, P. Suquet, A model-reduction approach to the micromechanical analysis of polycrystalline materials, *Comput. Mech.* 57 (3) (2016) 483–508.
- [86] C. Gu, QLMOR: A projection-based nonlinear model order reduction approach using quadratic-linear representation of nonlinear systems, *IEEE Trans. Comput.-Aided Des. Integr. Circuits Syst.* 30 (2011) 1307–1320.
- [87] B. Klimkeit, S. Castagnet, Y. Nadot, A. El Habib, G. Benoit, S. Bergamo, C. Dumas, S. Achard, Fatigue damage mechanisms in short fiber reinforced PBT+PET GF30, *Mater. Sci. Eng. A* 528 (2011) 1577–1588.
- [88] B. Halphen, Q.S. Nguyen, Sur les matériaux standards généralisés, *J. Méc.* 14 (1975) 508–520.
- [89] Q.S. Nguyen, *Stability and Nonlinear Solid Mechanics*, Wiley, New York, 2000.
- [90] M. Ortiz, L. Stainier, The variational formulation of viscoplastic constitutive updates, *Comput. Methods Appl. Mech. Engrg.* 171 (1999) 419–444.
- [91] C. Miehe, Strain-driven homogenization of inelastic microstructures and composites based on an incremental variational formulation, *Internat. J. Numer. Methods Engrg.* 55 (2002) 1285–1322.
- [92] N. Bakhvalov, G. Panasenko, *Homogenisation: Averaging Processes in Periodic Media*, Springer, Netherland, 1989.
- [93] R. Herzog, C. Meyer, G. Wachsmuth, Integrability of displacement and stresses in linear and nonlinear elasticity with mixed boundary conditions, *J. Math. Anal. Appl.* 382 (2) (2011) 802–813.
- [94] F. Becker, *Entwicklung einer Beschreibungsmethodik für das mechanische Verhalten unverstärkter Thermoplaste bei hohen Deformationsgeschwindigkeiten* (Ph.D. thesis), Martin-Luther-Universität Halle-Wittenberg, 1976.
- [95] S.G. Advani, C.L. Tucker, The use of tensors to describe and predict fiber orientation in short fiber composites, *J. Rheol.* 31 (8) (1987) 751–784.
- [96] M. Schneider, The sequential addition and migration method to generate representative volume elements for the homogenization of short fiber reinforced plastics, *Comput. Mech.* 59 (2017) 247–263.
- [97] H.H. Bauschke, P.L. Combettes, *Convex Analysis and Monotone Operator Theory in Hilbert Spaces*, second ed., in: CMS Books in Mathematics, Springer, New York, 2017.
- [98] K. Carlberg, C. Farhat, A low-cost, goal-oriented 'compact proper orthogonal decomposition' bases for model reduction of static systems, *Internat. J. Numer. Methods Engrg.* 86 (2011) 381–402.
- [99] L. Fick, Y. Maday, A.P. Patera, T. Tadei, A stabilized POD model for turbulent flows over a range of Reynolds numbers: optimal parametersampling and constrained projection, *J. Comput. Phys.* 371 (2018) 214–243.
- [100] M. Schneider, F. Ospald, M. Kabel, Computational homogenization of elasticity on a staggered grid, *Internat. J. Numer. Methods Engrg.* 105 (9) (2016) 693–720.
- [101] M. Schneider, A dynamical view of nonlinear conjugate gradient methods with applications to FFT-based computational micromechanics, *Comput. Mech.* 66 (2020) 239–257.
- [102] M. Kabel, T. Böhlke, M. Schneider, Efficient fixed point and Newton–Krylov solvers for FFT-based homogenization of elasticity at large deformations, *Comput. Mech.* 54 (2014) 1497–1514.
- [103] *FeelMath*, *FeelMath*, 2017, Fraunhofer Institute for Industrial Mathematics <http://www.itwm.fraunhofer.de/en/fraunhofer-itwm.html>, Kaiserslautern, Germany.
- [104] J. Bezanson, A. Edelman, S. Karpinski, V.B. Shah, Julia: A fresh approach to numerical computing, *SIAM Rev.* 59 (1) (2017) 65–98.
- [105] T. Böhlke, C. Brüggemann, Graphical representation of the generalized Hooke's law, *Tech. Mech.* 21 (2) (2001) 145–158.
- [106] T. Kanit, S. Forst, I. Galliet, V. Mounoury, D. Jeulin, Determination of the size of the representative volume element for random composites: statistical and numerical approach, *Int. J. Solids Struct.* 40 (2003) 3647–3679.
- [107] *Abaqus/Standard*, Dassault Systèmes Simulia <https://www.3ds.com/products-services/simulia/products/abaqus/>.
- [108] R.T. Rockafellar, *Convex Analysis*, Princeton University Press, Princeton, 1970.